Modeling deformation banding in dense and loose fluid-saturated sands

José E. Andrade[a*], Ronaldo I. Borja[b†]

[a]*Department of Civil and Environmental Engineering, Northwestern University,*
Evanston, IL 60208, USA

[b]*Department of Civil and Environmental Engineering, Stanford University, Stanford, CA 94305, USA*

Abstract

Balance of mass and linear momentum of a solid-fluid mixture furnish a complete set of equations from which the displacements of the solid matrix and the pore pressures can be resolved for the case of quasi-static loading, resulting in the so-called $\boldsymbol{u} - p$ Galerkin formulation. In this work, a recently proposed model for dense sands is utilized to model the effective stress response of the solid matrix appearing in the balance of linear momentum equation. In contrast with other more traditional models, inherent inhomogeneities in the porosity field at the meso-scale are thoroughly incorporated and coupled with the macroscopic laws of mixture theory. Also, the hydraulic conductivity is naturally treated as a function of the porosity in the solid matrix, allowing for a more realistic representation of the physical phenomenon. The aforementioned balance laws are cast into a fully nonlinear finite element program utilizing isoparametric elements satisfying the Babuška-Brezzi stability condition. Criteria for the onset of localization under locally drained and locally undrained conditions are derived and utilized to detect instabilities. Numerical simulations on dense and loose sand specimens are performed to study the effects of inhomogeneities on the stability of saturated porous media at the structural level.

1 Introduction

Deformation banding is one of the most common failure modes in geomaterials such as rock, concrete, and soil. It is well known that appearance of bands of intense localized deformation significantly reduces the load-carrying capacity of any structure that develops them [1, 2]. Furthermore, when dealing with fluid-saturated geomaterials, the interplay between the contraction/dilation of pores and development of pore fluid pressures is expected to influence not only the strength of the solid matrix but also its ability to block or transport such fluids [3]. Accurate and thorough simulation of these phenomena (i.e., deformation banding and fluid flow) requires numerical models capable of capturing fine-scale mechanical processes such as mineral particle rolling and sliding in granular soils and the coupling between porosity and relative permeability. Until recently, these processes could not even be observed in the laboratory. Numerical models could only interpret material behavior as a macroscopic process and were, therefore, unable to model the very complex behavior of saturated geomaterials accurately.

In this paper, we study the deformation-diffusion behavior of a two-phase system of soil and fluid. It is well known that the coupling between the mechanical behavior of the underlying drained solid and the fluid flow can lead to sharply distinct behavior of the overall mixed system. For instance, dilative saturated rock masses can lead to a phenomenon called 'dilatant hardening', which, as the name implies, tends to delay the onset of strain localization because effective pressures tend to increase and hence strengthen the sample [4–6]. On the other hand, relatively loose sands tend to compact when sheared. Therefore, when pores compact faster than the rate at which fluids can escape, pore fluid pressure increases and the effective pressure decreases, leading to a phenomenon known in the geotechnical community as 'liquefaction' [7–9]. Consequently, it is important to study the deformation-diffusion behavior in saturated granular media taking into account the effect of pore contraction/dilation and its influence on the relative density and permeability of the solid matrix. This is accomplished in this study.

Even though the interplay between fluid flow and solid deformation using finite elements has been studied before, the focus of models dealing with fully saturated and partially sat-

urated soils has been on 'homogeneous' material response [10–19]. This has been a natural approach given the fact that the technology to infer material inhomogeneities in the laboratory has only been recently developed. Therefore, numerical models dealing with the simulation of strain localization have either imposed inhomogeneous deformation fields (e.g., [10–12]) or introduced arbitrary weaknesses in the otherwise pristine specimens (e.g., [20–23]).

New advances in laboratory experimentation, such as X-Ray Computed Tomography (CT) and Digital Image Correlation (DIC) techniques, allow accurate observation of key parameters associated with material strength and provide the motivation for the development of more realistic models that incorporate information at a scale finer than specimen scale (see works in [24–26] for applications of X-Ray CT and [27, 28] for applications of DIC). In this paper, we adopt a refined constitutive model based on a meso-scale description of the porosity to simulate the development (location and direction) of deformation bands on saturated samples of sand. The effective stress behavior of the granular material is assumed to be governed by an elastoplastic model for sands developed by the authors in [29, 30]. The ability of the model to incorporate data depicting the inherent inhomogeneities in samples of sand at the meso-scale provides a natural and realistic source of inhomogeneity that, as we shall demonstrate subsequently, affects the stability and flow characteristics of sand specimens. As a matter of terminology the 'meso-scale' here refers to a scale smaller than specimen size but larger than particle size. In a typical sample encountered in the laboratory, the meso-scale refers to the millimeter scale.

The constitutive model for the effective stresses is a member of the critical state plasticity family of models. It is based on an original model proposed by Jefferies in [31] and extended by the authors in [29, 30]. Two main features distinguish this model from its critical state predecessors. First, the yield surface is allowed to 'detach' from the critical state line by introducing a state parameter ψ [32], allowing a state point to lie either above or below the critical state line (CSL). Through the state parameter ψ we are able to prescribe spatial values of porosity across the sample, which constitutes the connection to the meso-scale. Second, the model features a nonassociative flow rule and a three stress-invariant formulation, for

3

capturing important features of sand behavior [33].

The model for the two-phase system is based on the theory of mixtures [34, 35], which serves as the underlying theoretical block to develop balance laws for multi-phase bodies. Saturated granular media is modeled as a two-phase system composed of a solid phase and a fluid phase. This study extends the work of Li et al. [36] who considered *elastic* expulsion of fluids at finite strain and also extends the work by Armero [10] who looked at the strain localization behavior of *homogeneous* saturated samples of soil—obeying a generalized Drucker-Prager constitutive model—under boundary conditions favoring inhomogeneous deformations. Furthermore, here the fluid content is not decomposed into elastic and plastic parts as the porosity field is naturally coupled to the elastoplastic formulation emanating from the constitutive law for the porous matrix. The numerical implementation also differs from that of Armero [10] as it does not rely on the operator split technique, but rather solves the coupled system of nonlinear equations directly. It is worthwhile noting that Armero and Callari [37] and Callari and Armero [38] expanded the work by Armero [10] by developing a strong discontinuity model to model deformation banding in homogeneous saturated media at finite strains.

In this work, fluid-saturated porous media is modeled using nonlinear continuum mechanics and a novel constitutive model for sands. Furthermore, the effect of porosity is also accounted for by utilizing the Kozeny-Carman equation which relates the intrinsic permeability to the porosity [39]. The objective of this paper is to study the effect of fluctuations in porosity at the meso-scale on the stability and transport properties of samples of dense and loose sand analyzed as boundary-value problems.

Using the balance laws for the system, along with the concept of effective stresses, the strong form of the deformation-diffusion problem at finite deformations is developed. The variational form is obtained as a two-field mixed formulation where the displacements in the solid matrix $\boldsymbol{u}$ and the Cauchy fluid pressures p serve as basic unknowns. Thus, a classical $\boldsymbol{u} - p$ formulation is obtained and discretized in space using elements satisfying the Babuška-Brezzi stability condition [40, 41]. The linearization of the variational equations serve as the

building block to develop expressions for the acoustic tensor for two extreme cases: the case of locally drained behavior and the case of locally undrained behavior. These expressions for the acoustic tensor are then utilized in the analysis of localization of strain for a fully saturated medium.

The structure of the paper is as follows. In Section 2 the conservation of mass and linear momentum equations for a two-phase mixture are derived. Section 3 describes the constitutive framework utilized in the formulation. In particular, the concept of effective stress is introduced and the model governing the effective stresses is briefly described. Darcy's law is presented as the fundamental constitutive equation for fluid flow. In Section 4, the finite element solution procedure is presented and the linearization of the variational equations is addressed in detail. Section 5 addresses the extreme criteria for localization in fluid-saturated media. The framework described above is then used in a series of numerical examples presented in Section 6, where it is shown that the stability and flow properties of samples of sand are profoundly influenced by meso-scale inhomogeneities in the initial porosity field.

As for notations and symbols used in this paper, bold-faced letters denote tensors and vectors; the symbol '·' denotes an inner product of two vectors (e.g. $\boldsymbol{a} \cdot \boldsymbol{b} = a_i b_i$), or a single contraction of adjacent indices of two tensors (e.g. $\boldsymbol{c} \cdot \boldsymbol{d} = c_{ij} d_{jk}$); the symbol ':' denotes an inner product of two second-order tensors (e.g. $\boldsymbol{c} : \boldsymbol{d} = c_{ij} d_{ij}$), or a double contraction of adjacent indices of tensors of rank two and higher (e.g. $\boldsymbol{C} : \boldsymbol{\epsilon}^{\mathrm{e}} = C_{ijkl} \epsilon_{kl}^{\mathrm{e}}$); the symbol '$\otimes$' denotes a juxtaposition, e.g., $(\boldsymbol{a} \otimes \boldsymbol{b})_{ij} = a_i b_j$. Finally, for any symmetric second order tensors $\boldsymbol{\alpha}$ and $\boldsymbol{\beta}$, $(\boldsymbol{\alpha} \otimes \boldsymbol{\beta})_{ijkl} = \alpha_{ij} \beta_{kl}$, $(\boldsymbol{\alpha} \oplus \boldsymbol{\beta})_{ijkl} = \beta_{ik} \alpha_{jl}$, and $(\boldsymbol{\alpha} \ominus \boldsymbol{\beta})_{ijkl} = \alpha_{il} \beta_{jk}$.

2   Balance laws: conservation of mass and linear momentum

Consider a two-phase mixture of solids and fluid. The balance equations are obtained by invoking the classical mixture theory (see for example the works in [34, 35]). Within this context, each α-phase ($\alpha =$ s, f, for solid and fluid, respectively) or constituent occupies a volume fraction, $\phi^{\alpha} := V_{\alpha}/V$, where V_{α} is the volume occupied by the α-phase and $V = V_{\mathrm{s}} + V_{\mathrm{f}}$

is the total volume of the mixture. Naturally,

$$\phi^{\mathrm{s}} + \phi^{\mathrm{f}} = 1. \tag{2.1}$$

The total mass of the mixture is defined by the mass contribution from each phase i.e., $M = M_{\mathrm{s}} + M_{\mathrm{f}}$. The inherent or true mass density for the α-phase is defined as $\rho_\alpha := M_\alpha/V_\alpha$. Also, the apparent or partial mass density is given by $\rho^\alpha = \phi^\alpha \rho_\alpha$. Therefore, the total mass density is given by

$$\rho = \rho^{\mathrm{s}} + \rho^{\mathrm{f}}. \tag{2.2}$$

Furthermore, both phases are assumed to be superimposed on top of each other and hence, a point $\boldsymbol{x}$ in the mixture is occupied by both solid and fluid simultaneously.

From this point forward, all inherent or true quantities pertaining to the α-phase are designated with a subscript, whereas apparent or partial quantities are designated with a superscript as a general notation.

2.1   Balance of mass

In deriving the balance laws, it is relevant to pose all time derivatives following a particular phase. From Figure 1, we note that the current configuration of the mixture in a region Ω is defined by the mapping of the solid-phase $\boldsymbol{\varphi}_{\mathrm{s}}(\boldsymbol{X}_{\mathrm{s}}, t)$, where $\boldsymbol{X}_{\mathrm{s}} \equiv \boldsymbol{X}$ is the position vector in the reference configuration $\Omega_0^{\mathrm{s}} \equiv \Omega_0$, and the mapping of the fluid-phase $\boldsymbol{\varphi}_{\mathrm{f}}(\boldsymbol{X}_{\mathrm{f}}, t)$, where $\boldsymbol{X}_{\mathrm{f}}$ is the position vector in the reference configuration Ω_0^{f}. Hence, it is convenient to define the total time-derivative following the α-phase such that

$$\frac{\mathrm{d}^\alpha\left(\square\right)}{\mathrm{d}t} = \frac{\partial\left(\square\right)}{\partial t} + \nabla^{\boldsymbol{x}}\left(\square\right) \cdot \boldsymbol{v}_\alpha, \tag{2.3}$$

where $\nabla^{\boldsymbol{x}}\left(\square\right) \equiv \partial\square/\partial\boldsymbol{x}$ is the gradient operator with respect to the current configuration Ω and $\boldsymbol{v}_\alpha \equiv \partial\boldsymbol{\varphi}_\alpha/\partial t$ is the velocity vector of the α-phase. For simplicity of notation and where there is no room for ambiguity, we drop the subscripts and superscripts for all quantities pertaining to the solid-phase, as we will write all balance laws following this phase. It is thus
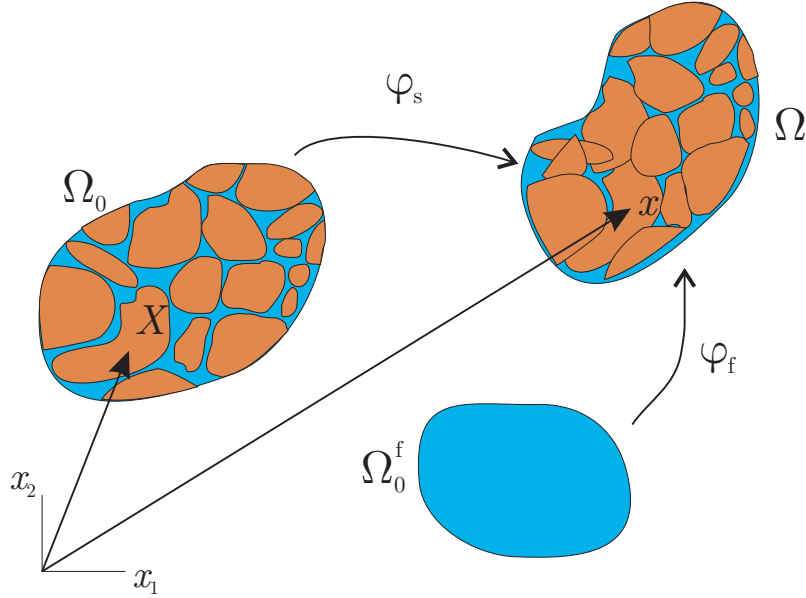
Figure 1: Current configuration Ω mapped from respective solid and fluid reference configurations.

straight-forward to check the identity

$$\frac{\mathrm{d}^{\mathrm{f}}\,(\square)}{\mathrm{d}t} = \frac{\mathrm{d}\,(\square)}{\mathrm{d}t} + \nabla^{\boldsymbol{x}}\,(\square) \cdot \tilde{\boldsymbol{v}}, \tag{2.4}$$

where $\tilde{\boldsymbol{v}} := \boldsymbol{v}_{\mathrm{f}} - \boldsymbol{v}$ is the relative velocity vector and $\mathrm{d}/\mathrm{d}t\,(\square) \equiv \dot{\overline{(\square)}}$ is the total material time derivative following the solid-phase.

Consider the expression for the total mass of α-phase in the current configuration i.e.,

$$m^{\alpha} \equiv \int_{\Omega} \phi^{\alpha}\rho_{\alpha}\,\mathrm{d}\Omega = \int_{\Omega_0^{\alpha}} \phi^{\alpha}\rho_{\alpha}J_{\alpha}\,\mathrm{d}\Omega_0^{\alpha}, \qquad \alpha = \mathrm{s}, \mathrm{f}, \tag{2.5}$$

which has been pulled back to the reference configuration of the α-phase via the mapping $\boldsymbol{\varphi}_{\alpha}^{-1}$ and where $J_{\alpha} = \det \boldsymbol{F}_{\alpha}$ is the Jacobian of the deformation gradient tensor $\boldsymbol{F}_{\alpha} \equiv \partial\boldsymbol{\varphi}_{\alpha}/\partial\boldsymbol{X}_{\alpha}$. If there is no production of α-phase mass and there are no mass exchanges amongst phases, conservation of mass implies

$$\frac{\mathrm{d}^{\alpha}}{\mathrm{d}t}m^{\alpha} = \int_{\Omega_0^{\alpha}} \frac{\mathrm{d}^{\alpha}}{\mathrm{d}t}\,(\phi^{\alpha}\rho_{\alpha}J_{\alpha})\,\mathrm{d}\Omega_0^{\alpha} = 0, \qquad \alpha = \mathrm{s}, \mathrm{f}, \tag{2.6}$$

7

which after classical continuity arguments yields the localized form of the conservation of mass for the α-phase

$$\frac{\mathrm{d}^\alpha}{\mathrm{d}t}\rho^\alpha + \rho^\alpha\,\nabla^{\boldsymbol{x}}\!\cdot\boldsymbol{v}_\alpha = 0, \tag{2.7}$$

where $\nabla^{\boldsymbol{x}}\!\cdot(\Box)$ is the divergence operator with respect to the current configuration. Making use of equation (2.7) and identity (2.4) the conservation of mass equation for the solid and fluid phases are, respectively,

$$\dot{\rho}^{\mathrm{s}} + \rho^{\mathrm{s}}\,\nabla^{\boldsymbol{x}}\!\cdot\boldsymbol{v} \;=\; 0 \tag{2.8a}$$

$$\dot{\rho}^{\mathrm{f}} + \rho^{\mathrm{f}}\,\nabla^{\boldsymbol{x}}\!\cdot\boldsymbol{v} \;=\; -\,\nabla^{\boldsymbol{x}}\!\cdot\boldsymbol{q}, \tag{2.8b}$$

where $\boldsymbol{q} \equiv \rho^{\mathrm{f}}\tilde{\boldsymbol{v}}$ is the Eulerian relative flow vector of the fluid phase with respect to the solid matrix. Adding equations (2.8a) and (2.8b), we get the basic conservation of mass equation for the system, i.e.,

$$\boxed{\dot{\rho}_0 = -J\,\nabla^{\boldsymbol{x}}\!\cdot\boldsymbol{q},} \tag{2.9}$$

where $\rho_0 \equiv J\rho$ is the pull-back mass density of the mixture in the reference configuration. It is clear from the above equation that in the case of locally undrained deformations (i.e., when both phases of the mixture move as one) $\boldsymbol{q} \approx 0$ and thus the relative mass flux term in the right-hand side drops out and the classical conservation of mass for a mono-phase body is captured.

Equations (2.8a) and (2.8b) are typically simplified by recalling the definition of the partial densities and introducing the bulk modulus. For barotropic flows, there exists a functional relationship of the form $f_\alpha\,(p_\alpha, \rho_\alpha) = 0$, where p_α is the intrinsic Cauchy pressure in the α-phase or the force acting on this phase per unit area of the same phase [36, 42]. Thus, it is meaningful to define the bulk modulus of the alpha phase such that

$$K_\alpha = \rho_\alpha \frac{\mathrm{d}p_\alpha}{\mathrm{d}\rho_\alpha}, \qquad \alpha = \mathrm{s}, \mathrm{f}, \tag{2.10}$$

and therefore equations (2.8a) and (2.8b) can then be rewritten, respectively, as

$$\dot{\phi}^{\mathrm{s}} + \phi^{\mathrm{s}} \left(\frac{\dot{p}_{\mathrm{s}}}{K_{\mathrm{s}}} + \nabla^{\boldsymbol{x}} \!\cdot \boldsymbol{v} \right) \;=\; 0 \tag{2.11a}$$

$$\dot{\phi}^{\mathrm{f}} + \phi^{\mathrm{f}} \left(\frac{\dot{p}_{\mathrm{f}}}{K_{\mathrm{f}}} + \nabla^{\boldsymbol{x}} \!\cdot \boldsymbol{v} \right) \;=\; -\frac{1}{\rho_{\mathrm{f}}} \nabla^{\boldsymbol{x}} \!\cdot \boldsymbol{q}. \tag{2.11b}$$

Adding the last two equations and recalling equation (2.1), we get

$$\phi^{\mathrm{s}} \frac{\dot{p}_{\mathrm{s}}}{K_{\mathrm{s}}} + \phi^{\mathrm{f}} \frac{\dot{p}_{\mathrm{f}}}{K_{\mathrm{f}}} + \nabla^{\boldsymbol{x}} \!\cdot \boldsymbol{v} = -\frac{1}{\rho_{\mathrm{f}}} \nabla^{\boldsymbol{x}} \!\cdot \boldsymbol{q}. \tag{2.12}$$

The above equation can be expressed in terms of the Kirchhoff intrinsic pressures by recalling the relationship between the Kirchhoff and Cauchy stress tensors, i.e., $\boldsymbol{\tau}_{\alpha} \equiv J \boldsymbol{\sigma}_{\alpha}$ and as a result the Kirchhoff pressure for the α-phase is defined as $\vartheta_{\alpha} = J p_{\alpha}$. Using the identity $\dot{J} = J \nabla^{\boldsymbol{x}} \!\cdot \boldsymbol{v}$ [43] we express equation (2.12) as

$$\phi^{\mathrm{s}} \frac{\dot{\vartheta}_{\mathrm{s}}}{K_{\mathrm{s}}} + \phi^{\mathrm{f}} \frac{\dot{\vartheta}_{\mathrm{f}}}{K_{\mathrm{f}}} + \dot{J} \left[1 - \frac{\phi^{\mathrm{s}}}{J} \frac{\vartheta_{\mathrm{s}}}{K_{\mathrm{s}}} - \frac{\phi^{\mathrm{f}}}{J} \frac{\vartheta_{\mathrm{f}}}{K_{\mathrm{f}}} \right] = -\frac{J}{\rho_{\mathrm{f}}} \nabla^{\boldsymbol{x}} \!\cdot \boldsymbol{q}. \tag{2.13}$$

Equation (2.13) is complete in the sense that neither constitutive nor kinematic assumptions have been introduced. In geomechanical applications, a typical and plausible assumption is to treat the solid phase as incompressible, and consequently $K_{\mathrm{s}} \to \infty$. Then, the *reduced* balance of mass equation for the mixture can be written as

$$\phi^{\mathrm{f}} \frac{\dot{\vartheta}_{\mathrm{f}}}{K_{\mathrm{f}}} + \dot{J} \left[1 - \frac{\phi^{\mathrm{f}}}{J} \frac{\vartheta_{\mathrm{f}}}{K_{\mathrm{f}}} \right] = -\frac{J}{\rho_{\mathrm{f}}} \nabla^{\boldsymbol{x}} \!\cdot \boldsymbol{q}. \tag{2.14}$$

Finally, we can write the Lagrangian balance of mass equation by making use of the Piola identity, i.e. $\nabla^{\boldsymbol{X}} \!\cdot \left(J \boldsymbol{F}^{-t} \right) = 0$ where $\nabla^{\boldsymbol{X}} \!\cdot (\square)$ is the divergence operator with respect to the reference configuration of the solid phase and the superscript 't' is the transpose operator. Thus,

$$J \nabla^{\boldsymbol{x}} \!\cdot \boldsymbol{q} = \nabla^{\boldsymbol{X}} \!\cdot \boldsymbol{Q}, \tag{2.15}$$

where $\boldsymbol{Q} \equiv J \boldsymbol{F}^{-1} \!\cdot \boldsymbol{q}$ is the Piola transform of the Eulerian vector $\boldsymbol{q}$. Therefore, the Lagrangian

9

balance of mass equation takes the form, cf. equation (2.9),

$$\boxed{\dot{\rho}_0 = -\nabla^{\boldsymbol{X}} \cdot \boldsymbol{Q}.}$$
(2.16)

2.2 Balance of linear momentum

At this point, it is necessary to introduce the concept of partial stresses in a more rigorous way. Let $\boldsymbol{\sigma}^{\alpha}$ denote the Cauchy partial stress tensor for the α-phase. The total Cauchy stress tensor is obtained from the sum [35, 44, 45]

$$\boldsymbol{\sigma} = \boldsymbol{\sigma}^{\mathrm{s}} + \boldsymbol{\sigma}^{\mathrm{f}}.$$
(2.17)

From the above definition, an expression for the partial Cauchy pressure or mean normal stress for the α-phase can be readily obtained, i.e. $p^{\alpha} \equiv -1/3 \operatorname{tr} \boldsymbol{\sigma}^{\alpha}$ and hence, the intrinsic Cauchy pressures can be defined such that

$$p_{\mathrm{s}} = -\frac{1}{3\phi^{\mathrm{s}}} \operatorname{tr} \boldsymbol{\sigma}^{\mathrm{s}} \qquad \text{and} \qquad p_{\mathrm{f}} = -\frac{1}{3\phi^{\mathrm{f}}} \operatorname{tr} \boldsymbol{\sigma}^{\mathrm{f}}.$$
(2.18)

Also, the associated first Piola-Kirchhoff partial stress tensor can be defined as $\boldsymbol{P}^{\alpha} = J\boldsymbol{\sigma}^{\alpha} \cdot \boldsymbol{F}^{-t}$, and the total first Piola-Kirchhoff stress tensor is given by

$$\boldsymbol{P} = \boldsymbol{P}^{\mathrm{s}} + \boldsymbol{P}^{\mathrm{f}}.$$
(2.19)

The linear momentum acting on the α-phase is given by [34, 35, 46]

$$\boldsymbol{l}^{\alpha} = \int_{\Omega} \rho^{\alpha} \boldsymbol{v}_{\alpha} \, \mathrm{d}\Omega,$$
(2.20)

whereas the resulting forces acting on the phase are [45]

$$\boldsymbol{r}^{\alpha} = \int_{\Omega} (\phi^{\alpha} \rho_{\alpha} \boldsymbol{g} + \phi^{\alpha} \boldsymbol{h}_{\alpha}) \, \mathrm{d}\Omega + \int_{\Gamma} \phi^{\alpha} \boldsymbol{t}_{\alpha} \, \mathrm{d}\Gamma,$$
(2.21)

10

where $\boldsymbol{g}$ is the gravity vector. The first term in (2.21) results from the body forces acting on the α-phase, the second term comes from the forces exerted on the α-phase from other phases in the mixture, and the third term emanates from the tractions imposed on the phase at the boundary Γ. Note that the partial traction is related to the partial Cauchy stress on the α-phase via the tetrahedron theorem i.e., $\boldsymbol{t}^\alpha \equiv \phi^\alpha \boldsymbol{t}_\alpha = \boldsymbol{\sigma}^\alpha \cdot \boldsymbol{n}$, where $\boldsymbol{n}$ is a unit vector normal to the surface Γ.

Balance of linear momentum on the α-phase necessitates

$$\frac{\mathrm{d}^\alpha}{\mathrm{d}t} \boldsymbol{l}^\alpha = \boldsymbol{r}^\alpha, \tag{2.22}$$

and after pull-back and push-forward operations and enforcing balance of mass, see equation (2.7), we get

$$\int_\Omega \rho^\alpha \boldsymbol{a}_\alpha \, \mathrm{d}\Omega = \boldsymbol{r}^\alpha, \tag{2.23}$$

where $\boldsymbol{a}_\alpha \equiv \mathrm{d}^\alpha \boldsymbol{v}^\alpha / \mathrm{d}t$ is the absolute acceleration vector for the α-phase. Once again, we can invoke localization arguments to get the point-wise version for the balance of linear momentum for the α-phase

$$\nabla^{\boldsymbol{x}} \cdot \boldsymbol{\sigma}^\alpha + \rho^\alpha \boldsymbol{g} + \phi^\alpha \boldsymbol{h}_\alpha = \rho^\alpha \boldsymbol{a}_\alpha, \tag{2.24}$$

which leads to the overall balance of linear momentum equation for the mixture i.e.,

$$\nabla^{\boldsymbol{x}} \cdot \boldsymbol{\sigma} + \rho \boldsymbol{g} = \rho \boldsymbol{a}_{\mathrm{s}} + \rho^{\mathrm{f}} \tilde{\boldsymbol{a}}, \tag{2.25}$$

where $\tilde{\boldsymbol{a}} \equiv \boldsymbol{a}_{\mathrm{f}} - \boldsymbol{a}_{\mathrm{s}}$ is the relative acceleration. In obtaining the above equation, the balance of linear momentum equations for both phases have been added and the fact that $\phi^{\mathrm{s}} \boldsymbol{h}_{\mathrm{s}} + \phi^{\mathrm{f}} \boldsymbol{h}_{\mathrm{f}} = \boldsymbol{0}$, since these are mutually-equilibrating internal forces, has been exploited. For the important case of quasi-static loading, all inertial forces are neglected and the equation of balance of linear momentum for the mixture reduces to the classical form

$$\boxed{\nabla^{\boldsymbol{x}} \cdot \boldsymbol{\sigma} + \rho \boldsymbol{g} = \boldsymbol{0}.} \tag{2.26}$$

In this work, only quasi-static loading conditions will be considered.

Finally, the Lagrangian form of the balance of linear momentum is easily obtained from its Eulerian counterpart, namely,

$$\nabla^{\boldsymbol{X}} \cdot \boldsymbol{P} + \rho_0 \boldsymbol{g} = \rho \boldsymbol{a}_\mathrm{s} + \rho^\mathrm{f} \tilde{\boldsymbol{a}}. \tag{2.27}$$

Accordingly, the Lagrangian balance of linear momentum for the system in the quasi-static range takes the form

$$\boxed{\nabla^{\boldsymbol{X}} \cdot \boldsymbol{P} + \rho_0 \boldsymbol{g} = \boldsymbol{0}.} \tag{2.28}$$

Remark 1. The equations of balance of mass and linear momentum derived above from basic principles of the mixture theory are identical to those presented by Borja in [45] and Li et al. in [36]. In fact, Borja [45] considers the case of a three-phase mixture by taking into account the gas phase also and develops a constitutive framework, but no boundary value problems are solved. The interested reader is referred to the work in [45] where the remaining balance laws for the multi-phase system are reported.

3 Constitutive framework

There is the need to establish a link between the state of stress and the displacements or deformations and between the flow vector and the fluid pressure in the porous media. These links are provided by constitutive relationships that we shall explicate in this section. In particular, the stresses are assumed to be a nonlinear function of the deformations via an elastoplastic constitutive response. On the other hand, the relative flow vector is related to the fluid pressure using Darcy's law.

3.1 The elastoplastic model for granular media

Analogous to the case of mono-phase materials, constitutive relations in fluid saturated porous media connect the deformations in the solid matrix to a suitable measure of stress. The relationship must connect so-called energy conjugate pairs of stress-strain measures. Consider

the general definition of effective stress for saturated conditions [47, 48]

$$\boldsymbol{\sigma}' = \boldsymbol{\sigma} + \left(1 - \frac{K}{K_\mathrm{s}}\right) p_\mathrm{f}\mathbf{1}, \tag{3.1}$$

where K is the bulk modulus of the solid matrix and $\mathbf{1}$ is the second-order identity tensor. Borja in [48] derived expression (3.1) using a strong discontinuity approach for the mechanical theory of porous media, and has shown that one suitable energy conjugate pair is furnished by the effective stress $\boldsymbol{\sigma}'$ and the symmetric part of the rate of deformation tensor for the solid matrix $\boldsymbol{d} \equiv \mathrm{sym}\,\boldsymbol{l}$, with $\boldsymbol{l} \equiv \nabla^{\boldsymbol{x}}\,\boldsymbol{v}$, and where we have dropped the subscript 's' from the velocity vector as there is no room for ambiguity.

For the case of interest herein, where the solid phase is assumed to be incompressible, the above expression for the effective stress reduces to the classical form introduced by Terzaghi [49], i.e.

$$\boldsymbol{\sigma}' = \boldsymbol{\sigma} + p\mathbf{1} \qquad \Longrightarrow \qquad \boldsymbol{\tau}' = \boldsymbol{\tau} + \vartheta\mathbf{1}, \tag{3.2}$$

where the expression on the right-hand-side has been obtained from direct application of the relationship between the Kirchhoff and the Cauchy stress (i.e., $\boldsymbol{\tau} = J\boldsymbol{\sigma}$). Also note the subscript 'f' has been dropped from the fluid-phase pressures for simplicity of notation. For incompressible solid grains, the balance of mass for the solid phase (cf. (2.11a)) necessitates $\dot{\phi}^\mathrm{s} + \phi^\mathrm{s}\,\nabla^{\boldsymbol{x}}\!\cdot\boldsymbol{v} = 0$ implying $\overline{(J\phi^\mathrm{s})} = 0$, and therefore

$$\phi^\mathrm{s} = \phi_0^\mathrm{s}/J \qquad \text{and} \qquad \phi^\mathrm{f} = 1 - \left(1 - \phi_0^\mathrm{f}\right)/J, \tag{3.3}$$

where ϕ_0^s and ϕ_0^f are the reference values of ϕ^s and ϕ^f when $J = 1$. Also, the bulk modulus for the fluid phase is assumed to be constant and hence recalling its definition allows us to obtain a relationship between the intrinsic fluid pressure and the intrinsic fluid density, i.e.

$$K_\mathrm{f} = \rho_\mathrm{f}\frac{\mathrm{d}p}{\mathrm{d}\rho_\mathrm{f}} = \text{constant} \qquad \Longrightarrow \qquad \rho_\mathrm{f} = \rho_\mathrm{f0}\exp\left(\frac{p - p_\mathrm{f0}}{K_\mathrm{f}}\right), \tag{3.4}$$

where ρ_f0 is the initial reference fluid mass density at initial pressure p_f0.

At this point, a constitutive framework governing the *effective* stress as a function of the solid matrix deformation can be introduced. Herein we assume the effective behavior of the granular material is governed by the three-invariant hyperelastoplastic model proposed by the authors in [29, 30]. Here, we summarize the salient features of the model.

The model is cast within the framework of nonlinear kinematics where the total deformation gradient is assumed to allow the multiplicative decomposition into elastic and plastic parts [50] i.e.,

$$\boldsymbol{F} = \boldsymbol{F}^{\mathrm{e}} \cdot \boldsymbol{F}^{\mathrm{p}}, \tag{3.5}$$

where $\boldsymbol{F}^{\mathrm{e}}$ and $\boldsymbol{F}^{\mathrm{p}}$ are defined as the elastic and plastic deformation gradient, respectively.

3.1.1 Isotropic hyperelasticity

Consider the principal elastic stretches emanating from $\boldsymbol{F}^{\mathrm{e}} \cdot \boldsymbol{N}^a = \lambda^a \boldsymbol{n}^a$ (no sum), where λ_a^{e} for $a = 1, 2, 3$ are the principal elastic stretches in the corresponding principal directions $\boldsymbol{N}^a$ and $\boldsymbol{n}^a$ in the intermediate and current configuration, respectively. Material isotropy is satisfied if the strain-energy function $\Psi = \Psi\left(\lambda_1^{\mathrm{e}}, \lambda_2^{\mathrm{e}}, \lambda_3^{\mathrm{e}}\right)$. The elastic region is assumed to be governed by the isotropic strain energy function proposed in [51] and utilized in modeling of granular bodies in [52, 53],

$$\Psi\left(\varepsilon_{\mathrm{v}}^{\mathrm{e}}, \varepsilon_{\mathrm{s}}^{\mathrm{e}}\right) = \tilde{\Psi}\left(\varepsilon_{\mathrm{v}}^{\mathrm{e}}\right) + \frac{3}{2}\mu^{\mathrm{e}}\varepsilon_{\mathrm{s}}^{\mathrm{e}\,2}, \tag{3.6}$$

where

$$\tilde{\Psi}\left(\varepsilon_{\mathrm{v}}^{\mathrm{e}}\right) = -p_0\hat{\kappa}\exp\omega, \qquad \omega = -\frac{\varepsilon_{\mathrm{v}}^{\mathrm{e}} - \varepsilon_{\mathrm{v}0}^{\mathrm{e}}}{\hat{\kappa}}, \qquad \mu^{\mathrm{e}} = \mu_0 + \frac{\alpha_0}{\hat{\kappa}}\tilde{\Psi}\left(\varepsilon_{\mathrm{v}}^{\mathrm{e}}\right). \tag{3.7}$$

The independent variables are the volumetric and deviatoric invariants of the elastic logarithmic stretch tensor, respectively,

$$\varepsilon_{\mathrm{v}}^{\mathrm{e}} = \varepsilon_1^{\mathrm{e}} + \varepsilon_2^{\mathrm{e}} + \varepsilon_3^{\mathrm{e}} \qquad \text{and} \qquad \varepsilon_{\mathrm{s}}^{\mathrm{e}} = \frac{1}{3}\sqrt{2\left[(\varepsilon_1^{\mathrm{e}} - \varepsilon_2^{\mathrm{e}})^2 + (\varepsilon_2^{\mathrm{e}} - \varepsilon_3^{\mathrm{e}})^2 + (\varepsilon_3^{\mathrm{e}} - \varepsilon_1^{\mathrm{e}})^2\right]}, \tag{3.8}$$

where $\varepsilon_a^{\mathrm{e}} \equiv \ln \lambda_a^{\mathrm{e}}$. The strain energy function is an invariant function of the elastic deformations only. The Kirchhoff effective stress tensor $\boldsymbol{\tau}'$ is coaxial with the left elastic Cauchy-Green

deformation tensor $b^{\mathrm{e}} \equiv F^{\mathrm{e}} \cdot F^{\mathrm{e}\,\mathrm{t}}$ and defined such that

$$\boldsymbol{\tau}' = 2\frac{\partial \Psi}{\partial b^{\mathrm{e}}} \cdot b^{\mathrm{e}}. \tag{3.9}$$

The above hyperelastic model produces pressure-dependent elastic bulk and shear moduli, a feature commonly observed in the laboratory. The elastic constants necessary for a full description of the elasticity are the reference strain $\varepsilon^{\mathrm{e}}_{\mathrm{v}\,0}$ and the reference pressure p_0 of the elastic compression curve, as well as the compressibility index $\hat{\kappa}$. The model produces coupled volumetric and deviatoric responses in the case $\alpha_0 \neq 0$ for which μ^{e} is a nonlinear function of the volumetric deformations. Otherwise, for $\alpha_0 = 0$ the responses are decoupled and the shear modulus $\mu^{\mathrm{e}} \equiv \mu_0$ is constant.

3.1.2 Plasticity for sands

We define the three invariants of the effective Kirchhoff stress tensor as

$$p' = \frac{1}{3}\operatorname{tr}\boldsymbol{\tau}', \qquad q = \sqrt{\frac{3}{2}}\|\boldsymbol{\xi}'\|, \qquad \frac{1}{\sqrt{6}}\cos 3\theta = \frac{\operatorname{tr}\boldsymbol{\xi}'^3}{\chi^3} \equiv y, \tag{3.10}$$

where $\boldsymbol{\xi}' = \boldsymbol{\tau}' - p'\mathbf{1}$ is the deviatoric component of the effective stress tensor $\boldsymbol{\tau}'$, and $\chi = \sqrt{\operatorname{tr}\boldsymbol{\xi}'^2}$. The quantity p' is called the mean normal effective stress and is assumed negative throughout. Further, θ is the Lode's angle whose values range from $0 \leq \theta \leq \pi/3$; it defines an angle on a deviatoric plane emanating from a tension corner.

From these three stress invariants we construct a yield surface of the form

$$F\left(\boldsymbol{\tau}', \pi_{\mathrm{i}}\right) = F\left(p', q, \theta, \pi_{\mathrm{i}}\right) = \zeta\left(\theta\right)q + p'\eta\left(p', \pi_{\mathrm{i}}\right) \tag{3.11}$$

where

$$\eta = \begin{cases} M\left[1 + \ln\left(\pi_{\mathrm{i}}/p'\right)\right] & \text{if} \quad N = 0 \\ M/N\left[1 - (1 - N)\left(p'/\pi_{\mathrm{i}}\right)^{N/(1-N)}\right] & \text{if} \quad N > 0. \end{cases} \tag{3.12}$$

The image stress $\pi_{\mathrm{i}} < 0$ controls the size of the yield surface; it is defined such that the stress ratio $\eta = -\zeta q/p = M$ when $p' = \pi_{\mathrm{i}}$. The parameter $N \geq 0$ determines the curvature of the

yield surface on a meridian plane and it typically has a value less than or equal to 0.4 for sands [31]. Lode's angle θ plays the role of the third stress invariant modifying the shape of the yield and plastic potential surfaces on a deviatoric plane through the function $\zeta = \zeta(\theta)$. Here we adopt the form proposed by Gudehus in [54] and Argyris et al. in [55], namely,

$$\zeta(\theta) = \frac{(1+\varrho) + (1-\varrho)\cos 3\theta}{2\varrho} \tag{3.13}$$

where ϱ is a constant parameter called ellipticity. The above function is only convex for $7/9 \leq \varrho \leq 1$ [56] and satisfies the boundary conditions: (a) $\zeta = 1/\varrho$ when $\theta = 0$ i.e., tension corner; and (b) $\zeta = 1$ when $\theta = \pi/3$ i.e., compression corner. The third invariant allows us to account for the fact that soils have less yield strength in triaxial extension than in compression.

Remark 2. We note in passing that in the present work we do not make use of the shape function proposed by Willam and Warnke [57] as it has been shown recently in [58] (and experienced first hand by the authors) that such shape function, shown in equation (12) in [29], leads to convergence problems in the material subroutine when ϱ gets small. Hence, to avoid loss of robustness in our numerical simulations, we only make use of the simple shape function presented above.

Similar to the yield surface, we can postulate a plastic potential function of the form

$$G(\boldsymbol{\tau}', \overline{\pi}_{\mathrm{i}}) = G(p', q, \theta, \overline{\pi}_{\mathrm{i}}) = \zeta(\theta)\, q + p'\overline{\eta}(p', \overline{\pi}_{\mathrm{i}}) \tag{3.14}$$

with

$$\overline{\eta} = \begin{cases} M\left[1 + \ln\left(\overline{\pi}_{\mathrm{i}}/p'\right)\right] & \text{if } \overline{N} = 0 \\ M/\overline{N}\left[1 - \left(1 - \overline{N}\right)\left(p'/\overline{\pi}_{\mathrm{i}}\right)^{\overline{N}/(1-\overline{N})}\right] & \text{if } \overline{N} > 0. \end{cases} \tag{3.15}$$

When $\overline{\pi}_{\mathrm{i}} = \pi_{\mathrm{i}}$ and $\overline{N} = N$, plastic flow is associative; otherwise, it is nonassociative in the volumetric sense. Additionally, from the multiplicative decomposition of the deformation

gradient, the additive decomposition of the velocity gradient $\boldsymbol{l}$ follows,

$$\boldsymbol{l} = \boldsymbol{l}^{\mathrm{e}} + \boldsymbol{l}^{\mathrm{p}} \qquad \Rightarrow \qquad \boldsymbol{d} = \boldsymbol{d}^{\mathrm{e}} + \boldsymbol{d}^{\mathrm{p}}, \tag{3.16}$$

where $\boldsymbol{d}^{\mathrm{e}} \equiv \mathrm{sym}\,\boldsymbol{l}^{\mathrm{e}}$, and $\boldsymbol{d}^{\mathrm{p}} \equiv \mathrm{sym}\,\boldsymbol{l}^{\mathrm{p}}$. Neglecting the plastic spin $\boldsymbol{\omega}^{\mathrm{p}}$ (see [59] for significance and consequences), we write the flow rule as

$$\boldsymbol{d}^{\mathrm{p}} = \dot{\lambda} \frac{\partial G}{\partial \boldsymbol{\tau}'}, \tag{3.17}$$

where $\dot{\lambda}$ is the so-called consistency parameter.

Finally, recall the definitions for the volumetric and deviatoric plastic strain rate invariants, respectively,

$$\dot{\varepsilon}_{\mathrm{v}}^{\mathrm{p}} = \mathrm{tr}\,\boldsymbol{d}^{\mathrm{p}} \qquad \text{and} \qquad \dot{\varepsilon}_{\mathrm{s}}^{\mathrm{p}} = \sqrt{\frac{2}{3}}\,\|\boldsymbol{d}^{\mathrm{p}} - 1/3\dot{\varepsilon}_{\mathrm{v}}^{\mathrm{p}}\boldsymbol{1}\|. \tag{3.18}$$

Also, consider the state parameter ψ_{i}, which is the distance between the specific volume of the sample and the specific volume at critical at the image pressure,

$$\psi_{\mathrm{i}} = v - v_{c0} + \widetilde{\lambda}\ln\left(-\pi_{\mathrm{i}}\right), \tag{3.19}$$

where v is the specific volume, v_{c0} is the reference specific volume at unit pressure, and $\widetilde{\lambda}$ is the plastic compressibility index. The state parameter ψ_{i} furnishes a link to the meso-scale by providing information about the relative density at a point in the sample. If $\psi_{\mathrm{i}} < 0$ the sample is denser than critical and if $\psi_{\mathrm{i}} > 0$ the sample is said to be looser than critical. In the case when $\psi_{\mathrm{i}} = 0$ the sample is at critical state. All of these parameters emanate from the critical state theory which postulates the existence of the critical state line [33, 60].

The hardening law, which relates the image pressure with the state of stress, the state parameter ψ_{i}, and the *deviatoric* component of plastic flow, reads

$$\dot{\pi}_{\mathrm{i}} = h\left(\pi_{\mathrm{i}}^{*} - \pi_{\mathrm{i}}\right)\dot{\varepsilon}_{\mathrm{s}}^{\mathrm{p}}, \tag{3.20}$$

where $\pi_i^* = \pi_i^* \left(p', \psi_i \right)$, and h is a constant material property, to be calibrated in the finite deformation regime. We note in passing that the above hardening law allows for correct qualitative capture of key features in both loose and dense sands by allowing hardening and softening plastic response. More details regarding the elastoplastic model for sands presented herein and its numerical implementation can be found in [29, 30, 61].

3.2 Darcy's law

The relative flow vector q is related to the Cauchy pore pressure via the Eulerian form of the classical Darcy's law [39, 46, 62]

$$ q = -\frac{1}{g} k \cdot \left[\nabla^x p - \gamma_f \right], \tag{3.21} $$

where $k \equiv k \gamma_f / \mu \mathbf{1}$ is the isotropic hydraulic conductivity tensor, the scalar k is the intrinsic permeability of the porous media, μ is the dynamic viscosity of the fluid, g is the gravitational acceleration constant, and $\gamma_f \equiv \rho_f g$ is the scalar specific weight of the fluid and $\gamma_f \equiv \rho_f g$ is its tensorial counterpart.

It is well documented throughout the literature that the intrinsic permeability can take the general form [39]

$$ k = f_1 \left(s \right) f_2 \left(\phi^f \right) d^2, \tag{3.22} $$

where s is a dimensionless parameter that expresses the effect of the shape of the solid grains, $f_1 \left(s \right)$ is called shape factor, $f_2 \left(\phi^f \right)$ is called the porosity factor and d is the effective diameter of the grains. One of the most widely used relationships for the permeability is the Kozeny-Carman permeability equation proposed by Kozeny [63] and Carman [64] namely (see [39]),

$$ k \left(\phi^f \right) = \frac{1}{180} \frac{\phi^{f\,3}}{\left(1 - \phi^f \right)^2} d^2, \tag{3.23} $$

which we will use herein to account for the effect of porosity and changes thereof in the Eulerian permeability tensor k.

For completeness of presentation, we obtain the Lagrangian expression for Darcy's law by

18
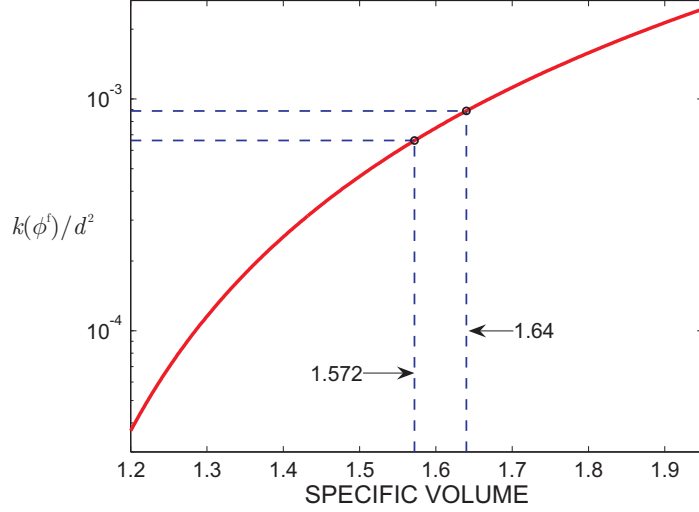
Figure 2: Nondimensional values of intrinsic permeability (i.e. k/d^2) as a function of specific volume v.

recalling the Piola transform of the relative flow vector,

$$\boldsymbol{Q} = J\boldsymbol{F}^{-1} \cdot \boldsymbol{q} = -\frac{1}{g}J\boldsymbol{F}^{-1} \cdot \boldsymbol{k} \cdot \left[\nabla^{\boldsymbol{x}} p - \boldsymbol{\gamma}_{\mathrm{f}}\right]. \tag{3.24}$$

By the same token, the expression can be further reduced by using the well-known relationship $\nabla^{\boldsymbol{X}}(\square) = \nabla^{\boldsymbol{x}}(\square) \cdot \boldsymbol{F}$ to obtain the fully Lagrangian form

$$\boldsymbol{Q} = -\frac{1}{g}\boldsymbol{K} \cdot \left[\nabla^{\boldsymbol{X}} p - \boldsymbol{F}^{\mathrm{t}} \cdot \boldsymbol{\gamma}_{\mathrm{f}}\right], \tag{3.25}$$

where $\boldsymbol{K} = J\boldsymbol{F}^{-1} \cdot \boldsymbol{k} \cdot \boldsymbol{F}^{-\mathrm{t}}$ is the pull-back hydraulic conductivity tensor.

Remark 3. Note that the intrinsic permeability is treated as a function of the *current* value of porosity ϕ^{f} and hence will need to be linearized accordingly (see equation 4.45). Figure 2 shows the variation of the intrinsic permeability with specific volume. For samples of globally undrained sand (as considered herein in the numerical simulations section), the variation in specific volume is not significant enough as to affect the results. However, in other boundary-value problems where compaction/dilation bands are allowed to form at large strains, changes in porosity can lead to changes in permeability of a few orders of magnitude [3].

19

4 Finite element implementation

In this section, the balance laws developed in Section 2 provide a complete set of governing equations, which allow for the solution of quasi-static deformation-diffusion boundary-value problems. We depart from the strong form of the problem, and develop the variational form and its linearized version which allows for optimal convergence of Newton-Raphson schemes, and finally present the classic matrix form known as the $\boldsymbol{u}-p$ formulation. The problem results in a parabolic system where the displacements of the solid phase and the pore-pressures are the basic unknowns in an updated Lagrangian finite element scheme [65].

4.1 The strong form

Consider the Lagrangian version of the strong form. Let Ω_0 be a simple body with boundary Γ_0 defined by the solid matrix in the reference configuration. Let $\boldsymbol{N}$ be the unit normal vector to the boundary Γ_0. We assume the boundary Γ_0 admits the decomposition [41]

$$
\begin{aligned}
\Gamma_0 &= \overline{\Gamma_0^d \cup \Gamma_0^t} = \overline{\Gamma_0^p \cup \Gamma_0^q}, \\
\emptyset &= \Gamma_0^d \cap \Gamma_0^t = \Gamma_0^p \cap \Gamma_0^q,
\end{aligned}
\tag{4.1}
$$

where Γ_0^d, Γ_0^t, Γ_0^p, and Γ_0^q are open sets and $\emptyset$ is the empty set. Figure 3 shows the region Ω_0 and its boundary Γ_0 decomposed as described above.
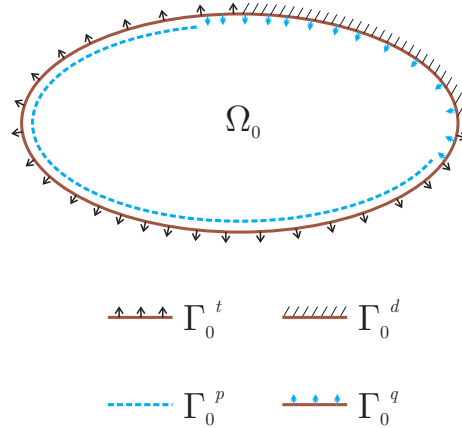
Figure 3: Reference domain Ω_0 with decomposed boundary Γ_0

The Lagrangian strong form for the quasi-static case and incompressible solid grains reads: find the displacements $\boldsymbol{u} \equiv \boldsymbol{x} - \boldsymbol{X} : \overline{\Omega}_0 \to \mathbb{R}^{n_{sd}}$ and the Cauchy pore-pressures $p : \overline{\Omega}_0 \to \mathbb{R}$ such that

$$
\begin{align}
\nabla^{\boldsymbol{X}} \cdot \boldsymbol{P} + \rho_0 \boldsymbol{g} &= \boldsymbol{0} && \text{in} && \Omega_0 && (4.2) \\
\dot{\rho}_0 + \nabla^{\boldsymbol{X}} \cdot \boldsymbol{Q} &= 0 && \text{in} && \Omega_0 && (4.3) \\
\boldsymbol{u} &= \overline{\boldsymbol{u}} && \text{on} && \Gamma_0^d && (4.4) \\
\boldsymbol{P} \cdot \boldsymbol{N} &= \boldsymbol{t} && \text{on} && \Gamma_0^t && (4.5) \\
p &= \overline{p} && \text{on} && \Gamma_0^p && (4.6) \\
\boldsymbol{Q} \cdot \boldsymbol{N} &= -Q && \text{on} && \Gamma_0^q && (4.7)
\end{align}
$$

where n_{sd} is the number of spatial dimensions to be considered, $\overline{\boldsymbol{u}}$ and $\overline{p}$ are the prescribed displacements and pressure on the Dirichlet boundaries Γ_0^d and Γ_0^p, respectively. By the same token, $\boldsymbol{t}$ and Q are the prescribed traction vector and influx with respect to the Neumann boundaries Γ_0^t and Γ_0^q, respectively. Finally, it is necessary to specify the initial conditions

$$
\boldsymbol{u}(\boldsymbol{X}, t = 0) = \boldsymbol{u}_0(\boldsymbol{X}), \qquad p(\boldsymbol{X}, t = 0) = p_0(\boldsymbol{X}), \tag{4.8}
$$

where $\boldsymbol{X}$ is a point in Ω_0.

4.2 The variational form

To define the weak or variational form, two classes of functions need to be characterized [41]. The first class is composed of trial solutions, which are required to satisfy the Dirichlet boundary conditions. The spaces of trial solutions for the displacement and pressure fields are, respectively [66]

$$
\begin{align}
\mathcal{S}_u &= \{\boldsymbol{u} : \Omega_0 \to \mathbb{R}^{n_{sd}} | \, u_i \in H^1, \; \boldsymbol{u} = \overline{\boldsymbol{u}} \text{ on } \Gamma_0^d\}, && (4.9) \\
\mathcal{S}_p &= \{p : \Omega_0 \to \mathbb{R} | \, p \in H^1, \; p = \overline{p} \text{ on } \Gamma_0^p\}, && (4.10)
\end{align}
$$

where H^1 is the space of Sobolev functions of first degree. The second class of functions are the weighting functions or variations. We require the weighting functions to vanish on Dirichlet boundaries. Thus, let the spaces of weighting functions associated with the displacement and pressure field be, respectively

$$\mathcal{V}_u \;=\; \{\boldsymbol{\eta} : \Omega_0 \to \mathbb{R}^{n_{sd}} |\; \eta_i \in H^1,\; \boldsymbol{\eta} = \boldsymbol{0} \;\text{ on }\; \Gamma_0^d\}, \tag{4.11}$$

$$\mathcal{V}_p \;=\; \{\psi : \Omega_0 \to \mathbb{R} |\; \psi \in H^1,\; \psi = 0 \;\;\text{ on }\; \Gamma_0^p\}. \tag{4.12}$$

Let $G : \mathcal{S}_u \times \mathcal{S}_p \times \mathcal{V}_u \to \mathbb{R}$ be given by

$$G\left(\boldsymbol{u}, p, \boldsymbol{\eta}\right) = \int_{\Omega_0} \left(\nabla^{\boldsymbol{X}} \boldsymbol{\eta} : \boldsymbol{P} - \rho_0 \boldsymbol{\eta} \cdot \boldsymbol{g}\right) \mathrm{d}\Omega_0 - \int_{\Gamma_0^t} \boldsymbol{\eta} \cdot \boldsymbol{t} \,\mathrm{d}\Gamma_0. \tag{4.13}$$

Under suitable smoothness conditions, $G\left(\boldsymbol{u}, p, \boldsymbol{\eta}\right) = 0$ can be shown to be equivalent to balance of linear momentum in the strong form, i.e., equations (4.2), (4.4) and (4.5). Similarly, let $H : \mathcal{S}_u \times \mathcal{S}_p \times \mathcal{V}_p \to \mathbb{R}$ take the form

$$H\left(\boldsymbol{u}, p, \psi\right) = \int_{\Omega_0} \left[\psi \dot{\rho}_0 - \nabla^{\boldsymbol{X}} \psi \cdot \boldsymbol{Q}\right] \mathrm{d}\Omega_0 - \int_{\Gamma_0^q} \psi Q \,\mathrm{d}\Gamma_0. \tag{4.14}$$

Once again, under suitable smoothness conditions, $H\left(\boldsymbol{u}, p, \psi\right) = 0$ can be shown to be equivalent to balance of mass in the strong form, i.e., equations (4.3), (4.6) and (4.7). Consequently, the Lagrangian weak form of the problem reads: find $\boldsymbol{u} \in \mathcal{S}_u$ and $p \in \mathcal{S}_p$ such that for all $\boldsymbol{\eta} \in \mathcal{V}_u$ and $\psi \in \mathcal{V}_p$

$$G\left(\boldsymbol{u}, p, \boldsymbol{\eta}\right) = H\left(\boldsymbol{u}, p, \psi\right) = 0. \tag{4.15}$$

It is our objective to develop an updated Lagrangian scheme and hence, we need to express the Lagrangian integrand of the above weak form in Eulerian form. We accomplish this by recalling the identities

$$\int_{\Omega_0} \nabla^{\boldsymbol{X}} \boldsymbol{\eta} : \boldsymbol{P} \,\mathrm{d}\Omega_0 = \int_{\Omega_0} \nabla^{\boldsymbol{x}} \boldsymbol{\eta} : \boldsymbol{\tau} \,\mathrm{d}\Omega_0, \qquad \int_{\Omega_0} \nabla^{\boldsymbol{X}} \psi \cdot \boldsymbol{Q} \,\mathrm{d}\Omega_0 = \int_{\Omega_0} J \nabla^{\boldsymbol{x}} \psi \cdot \boldsymbol{q} \,\mathrm{d}\Omega_0, \tag{4.16}$$

which we can insert into equations (4.13) and (4.14) above to get

$$G\left(\boldsymbol{u}, p, \boldsymbol{\eta}\right) = \int_{\Omega_0} \left(\nabla^{\boldsymbol{x}} \boldsymbol{\eta} : \boldsymbol{\tau} - J\rho\boldsymbol{\eta} \cdot \boldsymbol{g}\right) \mathrm{d}\Omega_0 - \int_{\Gamma_0^t} \boldsymbol{\eta} \cdot \boldsymbol{t} \, \mathrm{d}\Gamma_0, \tag{4.17}$$

and

$$H\left(\boldsymbol{u}, p, \psi\right) = \int_{\Omega_0} \left[\psi\dot{\rho}_0 - J\nabla^{\boldsymbol{x}} \psi \cdot \boldsymbol{q}\right] \mathrm{d}\Omega_0 - \int_{\Gamma_0^q} \psi Q \, \mathrm{d}\Gamma_0. \tag{4.18}$$

Finally, for the sake of compactness of presentation, we introduce the following notations,

$$g_1\left(\boldsymbol{u}, p\right) = \int_{\Omega_0} \nabla^{\boldsymbol{x}} \boldsymbol{\eta} : \left(\boldsymbol{\tau}' - Jp\mathbf{1}\right) \mathrm{d}\Omega_0, \tag{4.19a}$$

$$g_2\left(\boldsymbol{u}, p\right) = -\int_{\Omega_0} J\rho\boldsymbol{\eta} \cdot \boldsymbol{g} \, \mathrm{d}\Omega_0, \tag{4.19b}$$

$$g_{\text{ext}}\left(t\right) = \int_{\Gamma_0^t} \boldsymbol{\eta} \cdot \boldsymbol{t} \, \mathrm{d}\Gamma_0, \tag{4.19c}$$

and similarly

$$h_1\left(\boldsymbol{u}, p\right) = \int_{\Omega_0} \psi\dot{\rho}_0 \mathrm{d}\Omega_0, \tag{4.20a}$$

$$h_2\left(\boldsymbol{u}, p\right) = \int_{\Omega_0} \frac{J}{g} \nabla^{\boldsymbol{x}} \psi \cdot \boldsymbol{k} \cdot \left[\nabla^{\boldsymbol{x}} p - \boldsymbol{\gamma}_{\text{f}}\right] \mathrm{d}\Omega_0, \tag{4.20b}$$

$$h_{\text{ext}}\left(t\right) = \int_{\Gamma_0^q} \psi Q \, \mathrm{d}\Gamma_0, \tag{4.20c}$$

so that equation (4.15) implies

$$G\left(\boldsymbol{u}, p, \boldsymbol{\eta}\right) = g_{\text{ext}}\left(t\right) - g_1\left(\boldsymbol{u}, p\right) - g_2\left(\boldsymbol{u}, p\right), \tag{4.21}$$

$$H\left(\boldsymbol{u}, p, \psi\right) = h_{\text{ext}}\left(t\right) - h_1\left(\boldsymbol{u}, p\right) - h_2\left(\boldsymbol{u}, p\right). \tag{4.22}$$

4.2.1 Time integration and linearization of the variational form

Satisfaction of the weak form will entail solving a coupled nonlinear system of equations where the primary variables are the displacements $\boldsymbol{u}$ and the pore pressure p, hence the name $\boldsymbol{u} - p$ formulation. At the same time, the $\boldsymbol{u} - p$ formulation is resolved using an iterative Newton-Raphson procedure, which necessitates the system Jacobians or consistent tangents in closed

23

form for optimal asymptotic convergence rates. For the particular model proposed herein, it is possible to calculate such consistent tangents and thus attain optimal convergence rates. This is furnished by the fact that the elastoplastic model proposed is integrated within the return mapping algorithm framework [67], which allows for a closed form expression for the elastoplastic consistent tangent operator (see [29, 30, 61] for more details).

Consider the generalized trapezoidal family of methods [41] utilized in the solution of parabolic problems. The one-step scheme relies on the advancement of the solution at time station t_{n+1} from converged values at t_n, i.e.

$$
\left\{ \begin{array}{c} \boldsymbol{u} \\ p \end{array} \right\}_{n+1} = \left\{ \begin{array}{c} \boldsymbol{u} \\ p \end{array} \right\}_n + \Delta t \left(1 - \alpha\right) \left\{ \begin{array}{c} \dot{\boldsymbol{u}} \\ \dot{p} \end{array} \right\}_n + \Delta t \alpha \left\{ \begin{array}{c} \dot{\boldsymbol{u}} \\ \dot{p} \end{array} \right\}_{n+1} , \tag{4.23}
$$

where α is the integration parameter and $\Delta t \equiv t_{n+1} - t_n$ is the time step. Several classical schemes emanate for suitable choices of the integration parameter. For $\alpha = 0$ the scheme reduces to the explicit Euler algorithm, $\alpha = 1/2$ captures the Crank-Nicolson scheme, and $\alpha = 1$ reduces to the implicit backward Euler. For a detailed discussion about the stability and accuracy of the above-mentioned family please see [41]. With the purpose of obtaining a numerical scheme purely dependent on displacements $\boldsymbol{u}$ and pressure p, we integrate equation (4.22) using the trapezoidal family and obtain

$$
H_{\Delta t} \left(\boldsymbol{u}, p, \psi\right) = \int_{\Omega_0} \psi \Delta \rho_0 \, \mathrm{d}\Omega_0 \quad - \quad \Delta t \int_{\Omega_0} \underbrace{\left[\alpha J \, \nabla^{\boldsymbol{x}} \psi \cdot \boldsymbol{q} + \left(1 - \alpha\right) \left(J \, \nabla^{\boldsymbol{x}} \psi \cdot \boldsymbol{q}\right)_n\right]}_{\left(J \, \nabla^{\boldsymbol{x}} \psi \cdot \boldsymbol{q}\right)_{n+\alpha}} \mathrm{d}\Omega_0
$$

$$
- \quad \Delta t \int_{\Gamma_0^q} \psi \underbrace{\left(\alpha Q + \left(1 - \alpha\right) Q_n\right)}_{Q_{n+\alpha}} \mathrm{d}\Gamma_0, \tag{4.24}
$$

where $\Delta \rho_0 \equiv \rho_0 - \rho_{0\,n}$ and where we have omitted the '$n+1$' subscript for simplicity of notation. Similar to the results obtained above, the variational form implies

$$
H_{\Delta t} \left(\boldsymbol{u}, p, \psi\right) = h_{\text{ext}}^{\Delta t} \left(t\right) - h_1^{\Delta t} \left(\boldsymbol{u}, p\right) - h_2^{\Delta t} \left(\boldsymbol{u}, p\right), \tag{4.25}
$$

24

where

$$
\begin{aligned}
h_{\text{ext}}^{\Delta t}(t) &= \Delta t \int_{\Gamma_0^q} \psi Q_{n+\alpha} \mathrm{d}\Gamma_0 \\
h_1^{\Delta t}(\boldsymbol{u}, p) &= \int_{\Omega_0} \psi \Delta \rho_0 \, \mathrm{d}\Omega_0 \\
h_2^{\Delta t}(\boldsymbol{u}, p) &= -\Delta t \int_{\Omega_0} (J \nabla^{\boldsymbol{x}} \psi \cdot \boldsymbol{q})_{n+\alpha} \, \mathrm{d}\Omega_0.
\end{aligned}
\tag{4.26}
$$

The Newton-Raphson approach follows the standard procedure in which the governing equations from the weak form are expanded about a configuration $(\boldsymbol{u}^k, p^k)$ and only linear terms are kept i.e.,

$$
\begin{aligned}
0 = G(\boldsymbol{u}, p, \boldsymbol{\eta}) &\approx G\left(\boldsymbol{u}^k, p^k, \boldsymbol{\eta}\right) + \delta G\left(\boldsymbol{u}^k, p^k, \boldsymbol{\eta}\right), & (4.27) \\
0 = H_{\Delta t}(\boldsymbol{u}, p, \psi) &\approx H_{\Delta t}\left(\boldsymbol{u}^k, p^k, \psi\right) + \delta H_{\Delta t}\left(\boldsymbol{u}^k, p^k, \psi\right), & (4.28)
\end{aligned}
$$

hence, implying

$$
\begin{aligned}
-G\left(\boldsymbol{u}^k, p^k, \boldsymbol{\eta}\right) &= \delta G\left(\boldsymbol{u}^k, p^k, \boldsymbol{\eta}\right), & (4.29) \\
-H_{\Delta t}\left(\boldsymbol{u}^k, p^k, \psi\right) &= \delta H_{\Delta t}\left(\boldsymbol{u}^k, p^k, \psi\right). & (4.30)
\end{aligned}
$$

Therefore, the iterative strategy necessitates evaluation of the variations $\delta G\left(\boldsymbol{u}^k, p^k, \boldsymbol{\eta}\right)$ and $\delta H_{\Delta t}\left(\boldsymbol{u}^k, p^k, \psi\right)$. Note that equation (4.27) is solved at time t_{n+1} as implied by our notation.

The variation of $\delta G(\boldsymbol{u}, p, \boldsymbol{\eta})$ implies

$$
\delta G(\boldsymbol{u}, p, \boldsymbol{\eta}) = \delta g_{\text{ext}}(t) - \delta g_1(\boldsymbol{u}, p) - \delta g_2(\boldsymbol{u}, p),
\tag{4.31}
$$

where $\delta g_{\text{ext}}(t) = 0$ for deformation-independent tractions. Application of the chain rule then yields

$$
\delta g_1(\boldsymbol{u}, p) = \int_{\Omega_0} \left[\delta \nabla^{\boldsymbol{x}} \boldsymbol{\eta} : \left(\boldsymbol{\tau}' - Jp\mathbf{1}\right) + \nabla^{\boldsymbol{x}} \boldsymbol{\eta} : \delta \left(\boldsymbol{\tau}' - Jp\mathbf{1}\right)\right] \mathrm{d}\Omega_0,
\tag{4.32}
$$

where

$$\delta \, \nabla^{\boldsymbol{x}} \boldsymbol{\eta} \quad = \quad -\nabla^{\boldsymbol{x}} \boldsymbol{\eta} \cdot \nabla^{\boldsymbol{x}} \delta \boldsymbol{u}, \tag{4.33}$$

$$\delta \left(\boldsymbol{\tau}' - Jp\boldsymbol{1} \right) \quad = \quad \left(\boldsymbol{c}^{\mathrm{ep}} + \boldsymbol{\tau}' \oplus \boldsymbol{1} + \boldsymbol{\tau}' \ominus \boldsymbol{1} - Jp\boldsymbol{1} \otimes \boldsymbol{1} \right) : \nabla^{\boldsymbol{x}} \delta \boldsymbol{u} - J\delta p \boldsymbol{1} \tag{4.34}$$

$$\delta J \quad = \quad J \nabla^{\boldsymbol{x}} \cdot \delta \boldsymbol{u}. \tag{4.35}$$

The fourth-order tensor $\boldsymbol{c}^{\mathrm{ep}}$ is the elastoplastic consistent tangent operator emanating from the constitutive model described in Section 3. We get

$$\delta g_1 \left(\boldsymbol{u}, p \right) = \int_{\Omega_0} \left[\nabla^{\boldsymbol{x}} \boldsymbol{\eta} : \left(\boldsymbol{a}^{\mathrm{ep}} + Jp \left(\boldsymbol{1} \ominus \boldsymbol{1} - \boldsymbol{1} \otimes \boldsymbol{1} \right) \right) : \nabla^{\boldsymbol{x}} \delta \boldsymbol{u} - \nabla^{\boldsymbol{x}} \cdot \boldsymbol{\eta} J\delta p \right] \mathrm{d}\Omega_0, \tag{4.36}$$

where

$$\boldsymbol{a}^{\mathrm{ep}} \equiv \boldsymbol{c}^{\mathrm{ep}} + \boldsymbol{\tau}' \oplus \boldsymbol{1} \tag{4.37}$$

is the total elastoplastic tangent operator and $\mathcal{L}_{\boldsymbol{v}} \boldsymbol{\tau}' = \boldsymbol{c}^{\mathrm{ep}} : \boldsymbol{d}$ where $\mathcal{L}_{\boldsymbol{v}} \boldsymbol{\tau}'$ is the Lie derivative of the effective stress tensor $\boldsymbol{\tau}'$ (see Andrade and Borja [29] for notations). By the same token,

$$\begin{aligned} \delta g_2 \left(\boldsymbol{u}, p \right) \quad &= \quad -\int_{\Omega_0} \delta \rho_0 \boldsymbol{\eta} \cdot \boldsymbol{g} \, \mathrm{d}\Omega_0, \\ &= \quad -\int_{\Omega_0} J \left(\nabla^{\boldsymbol{x}} \cdot \delta \boldsymbol{u} + \frac{\phi^{\mathrm{f}}}{K_{\mathrm{f}}} \delta p \right) \boldsymbol{\eta} \cdot \boldsymbol{\gamma}_{\mathrm{f}} \, \mathrm{d}\Omega_0, \end{aligned} \tag{4.38}$$

where we have used equation (3.3), $\delta \rho_{\mathrm{s}} = 0$, and the following key results

$$\delta \phi^{\mathrm{f}} \quad = \quad \left(1 - \phi^{\mathrm{f}} \right) \nabla^{\boldsymbol{x}} \cdot \delta \boldsymbol{u}, \tag{4.39}$$

$$\delta \rho_{\mathrm{f}} \quad = \quad \frac{\rho_{\mathrm{f}}}{K_{\mathrm{f}}} \delta p. \tag{4.40}$$

Similarly,

$$\delta H_{\Delta t} \left(\boldsymbol{u}, p, \psi \right) = \delta h_{\mathrm{ext}}^{\Delta t} \left(t \right) - \delta h_1^{\Delta t} \left(\boldsymbol{u}, p \right) - \delta h_2^{\Delta t} \left(\boldsymbol{u}, p \right), \tag{4.41}$$

where $\delta h_{\text{ext}}^{\Delta t}(t) = 0$ for configuration- and pressure-independent mass flux. Thus,

$$\delta h_1^{\Delta t}(\boldsymbol{u}, p) = \int_{\Omega_0} \psi \delta \rho_0 \mathrm{d}\Omega_0 = \int_{\Omega_0} \psi \rho_{\text{f}} J \left(\nabla^{\boldsymbol{x}} \cdot \delta \boldsymbol{u} + \frac{\phi^{\text{f}}}{K_{\text{f}}} \delta p \right) \mathrm{d}\Omega_0. \tag{4.42}$$

Now, we compute

$$
\begin{aligned}
\delta h_2^{\Delta t}(\boldsymbol{u}, p) &= \alpha \Delta t \int_{\Omega_0} \frac{1}{g} \delta \left(J \nabla^{\boldsymbol{x}} \psi \cdot \boldsymbol{k} \right) \cdot \left(\nabla^{\boldsymbol{x}} p - \boldsymbol{\gamma}_{\text{f}} \right) \mathrm{d}\Omega_0 \\
&+ \alpha \Delta t \int_{\Omega_0} \frac{1}{g} J \nabla^{\boldsymbol{x}} \psi \cdot \boldsymbol{k} \cdot \delta \left(\nabla^{\boldsymbol{x}} p - \boldsymbol{\gamma}_{\text{f}} \right) \mathrm{d}\Omega_0,
\end{aligned}
\tag{4.43}
$$

where

$$\delta \nabla^{\boldsymbol{x}} \psi = - \nabla^{\boldsymbol{x}} \psi \cdot \nabla^{\boldsymbol{x}} \delta \boldsymbol{u} \tag{4.44}$$

$$\delta \boldsymbol{k} = \frac{1}{\mu} \left(k' \gamma_{\text{f}} \delta \phi^{\text{f}} + k \delta \rho_{\text{f}} g \right) \mathbf{1} \tag{4.45}$$

$$\delta \nabla^{\boldsymbol{x}} p = \nabla^{\boldsymbol{x}} \delta p - \nabla^{\boldsymbol{x}} p \cdot \nabla^{\boldsymbol{x}} \delta \boldsymbol{u} \tag{4.46}$$

$$\delta \boldsymbol{\gamma}_{\text{f}} = \delta \rho_{\text{f}} \boldsymbol{g}. \tag{4.47}$$

4.3 The matrix form

The spatial discretization is furnished by the classical Galerkin method whereby the displacement and the pressure fields are approximated by [41]

$$\boldsymbol{u} \approx \boldsymbol{N}\boldsymbol{d} + \boldsymbol{N}^\xi \boldsymbol{\xi}, \tag{4.48}$$

$$p \approx \overline{\boldsymbol{N}}\boldsymbol{p} + \boldsymbol{N}^\zeta \boldsymbol{\zeta}, \tag{4.49}$$

where $\boldsymbol{N}$ is the array of displacement shape functions, $\boldsymbol{d}$ is the vector of unknown displacements, $\boldsymbol{N}^\xi$ is the array of shape functions approximating the displacement boundary conditions, $\boldsymbol{\xi}$ is the vector of prescribed nodal displacements, $\overline{\boldsymbol{N}}$ is the array of pressure shape functions, $\boldsymbol{p}$ is the vector of unknown pore-pressures, $\boldsymbol{N}^\zeta$ is the array of shape functions approximating the pressure boundary conditions, and $\boldsymbol{\zeta}$ is the vector of prescribed nodal pore-pressures. Then, following the Galerkin recipe, the weighting functions are approximated

by

$$\eta \approx Nc, \tag{4.50}$$

$$\psi \approx \overline{N}\overline{c}, \tag{4.51}$$

where c and $\overline{c}$ are arbitrary constant vectors. The spatial and temporal discretization leads to the matrix form of the problem, which reads: find the vectors d and p such that

$$\left\{ \begin{array}{c} G_{\text{ext}} \\ H_{\text{ext}} \end{array} \right\} - \left\{ \begin{array}{c} G_{\text{int}} \\ H_{\text{int}} \end{array} \right\} \equiv \left\{ \begin{array}{c} R_g \\ R_h \end{array} \right\}, \tag{4.52}$$

where

$$G_{\text{ext}}(t) \equiv \int_{\Gamma_0^t} N^t t \, \mathrm{d}\Gamma_0, \tag{4.53}$$

$$G_{\text{int}}(d, p) \equiv \int_{\Omega_0} \left[B^t \left(\tau' - Jp\delta \right) - \rho_0 N^t g \right] \mathrm{d}\Omega_0, \tag{4.54}$$

and

$$H_{\text{ext}}(t) \equiv \Delta t \int_{\Gamma_0^q} \overline{N}^t Q_{n+\alpha} \, \mathrm{d}\Gamma_0, \tag{4.55}$$

$$H_{\text{int}}(d, p) \equiv \int_{\Omega_0} \left[\overline{N}^t \Delta \rho_0 - \Delta t \left(J\Gamma^t q \right)_{n+\alpha} \right] \mathrm{d}\Omega_0. \tag{4.56}$$

After algebraic manipulations, the Newton-Raphson incremental solution at the $k+1$ iteration is updated using

$$\left[\begin{array}{cc} K_g & \Phi_g \\ K_h + \alpha \Delta t \overline{K}_h & \Phi_h + \alpha \Delta t \overline{\Phi}_h \end{array} \right]_k \left\{ \begin{array}{c} \delta d \\ \delta p \end{array} \right\}_{k+1} = \left\{ \begin{array}{c} R_g \\ R_h \end{array} \right\}_k. \tag{4.57}$$

The reader is referred to Appendix A where a detailed presentation of the matrix form of the problem is given.

Remark 4. Some authors have pointed out the existence of numerical instabilities at the onset

of the deformation-diffusion problem when considering the case of incompressible fluid phase [68, 69]. In fact, Murad and Loula [68, 70] showed, in the context of linear elasticity, that at the onset of deformation the system is form-identical to the classical problem of incompressible elasticity or Stokes' flow in fluid mechanics. This is also true in the context of poroplasticity at large strains. The system can be shown to reduce to

$$
\begin{bmatrix} \hat{\boldsymbol{A}} & \hat{\boldsymbol{B}} \\ \hat{\boldsymbol{C}} & \boldsymbol{0} \end{bmatrix} \begin{Bmatrix} \delta\boldsymbol{u} \\ \delta\boldsymbol{p} \end{Bmatrix} = \begin{Bmatrix} \boldsymbol{F}_1 \\ \boldsymbol{F}_2 \end{Bmatrix}, \tag{4.58}
$$

and thus,

$$
\hat{\boldsymbol{C}}\hat{\boldsymbol{A}}^{-1}\hat{\boldsymbol{B}}\delta\boldsymbol{p} = \hat{\boldsymbol{C}}\hat{\boldsymbol{A}}^{-1}\boldsymbol{F}_1 - \boldsymbol{F}_2, \tag{4.59}
$$

where $\hat{\boldsymbol{A}}$ is a $nu \times nu$ square matrix, $\hat{\boldsymbol{B}}$ is a $nu \times nq$ rectangular matrix, and $\hat{\boldsymbol{C}}$ is a $nq \times nu$ matrix, with nu and nq representing the number of displacement and pore pressure unknowns, respectively. Hence, for $\hat{\boldsymbol{C}}\hat{\boldsymbol{A}}^{-1}\hat{\boldsymbol{B}}$ to have full rank, we must have $nu \geq np$. One way to avoid stability problems associated with this constraint is to satisfy the so-called Babuška-Brezzi condition (see [40, 41]). On the other hand, for the deformation-diffusion problem at hand, investigators have used stabilization techniques available to solve mixed problems. Wan in [69] used the Petrov-Galerkin technique proposed by Hughes et al. in [71] for solution of Stokes flow. Similarly, Mira et al [72] used Simo-Rifai elements [73] to obtain stable solutions for the deformation-diffusion problem. In this particular work, we only use mixed finite elements satisfying the Babuška-Brezzi stability condition.

5   Localization of saturated granular media

In this section, we will derive expressions for the Eulerian acoustic tensors corresponding to the locally (fully) drained and locally undrained conditions. These expressions are useful as they signal the loss of strong ellipticity of the corresponding drained and undrained global tangent operator. As in the classical case of mono-phase bodies, the onset of localization, as measured by the loss of positive definiteness in the acoustic tensor, can be used to define

29

the local direction of a shear band and maybe even as a switch for a change in the material behavior inside the band. Here, two extreme cases are considered. Firstly, we look at the case of a fully drained porous medium, which basically reduces back to the classical mono-phase theory. Secondly, we investigate the case of locally undrained behavior, where the global tangent is influenced by the bulk compressibility of the fluid phase, but relative flow is not present anywhere in the sample. In a way, this latter case is analogous to the drained case, but with a different underlying constitutive relation (one in which the fluid phase plays a role, but there is no diffusion). The global tangent $\boldsymbol{a}^{\mathrm{ep}}$ obtained in the previous section is used to obtain the drained and undrained localization criteria.

It is important to note that in general, saturated media behave somewhere in between locally drained and locally undrained conditions. For either extreme case, it is possible to write down an expression relating the total stress rate and the rate of deformation for the granular matrix i.e., $\delta\boldsymbol{P} = \mathbf{A} : \delta\boldsymbol{F}$, where $\mathbf{A}$ is the suitable (drained or undrained) first tangent operator with components $\mathrm{A}_{iJkL} := \partial P_{iJ}/\partial F_{kL}$ [43, 74]. Consequently, we require continuity of total tractions across the band and hence (cf., equation (2.35) in [74]),

$$[\![\mathbf{A} : \delta\boldsymbol{F}]\!] \cdot \boldsymbol{N} = \mathbf{0} \tag{5.1}$$

where $[\![\square]\!]$ is the jump operator across the band and $\boldsymbol{N}$ is the normal to an impending shear band in the reference configuration. Furthermore, by assuming the first tangent operator is continuous across the band we can write $[\![\mathbf{A} : \delta\boldsymbol{F}]\!] = \mathbf{A} : [\![\delta\boldsymbol{F}]\!]$. From [74] we get $[\![\dot{\boldsymbol{F}}]\!] = [\![\boldsymbol{V}]\!] \otimes \boldsymbol{N}/h_0$, where $[\![\boldsymbol{V}]\!]$ is the material velocity jump and h_0 is the (finite) thickness of the planar band in the reference configuration. Continuity of tractions requires

$$\frac{1}{h_0}\boldsymbol{\mathcal{A}} \cdot [\![\boldsymbol{V}]\!] = \mathbf{0}, \qquad \mathcal{A}_{ik} = N_J \mathrm{A}_{iJkL} N_L \tag{5.2}$$

For $h_0 \neq 0$, the necessary condition for localization is

$$\det \boldsymbol{\mathcal{A}} = 0 \tag{5.3}$$

with $\mathcal{A}$ as the Lagrangian acoustic tensor. Finally, pushing the Lagrangian acoustic tensor forward, we obtain the Eulerian acoustic tensor, i.e.

$$A_{ik} = n_j a_{ijkl} n_l \tag{5.4}$$

with $a_{ijkl} := F_{jJ} F_{lL} A_{iJkL}$ as the total spatial tangent operator and $\boldsymbol{n}$ is the normal to the deformation band in the current configuration. A standard argument then yields the Eulerian necessary condition for localization,

$$\det \boldsymbol{A} = 0. \tag{5.5}$$

Recall the relationship between the total First Piola Kirchhoff stress and the Kirchhoff stress, i.e. $\boldsymbol{P} = \boldsymbol{\tau} \cdot \boldsymbol{F}^{-t}$, which together with equation (3.1) yields

$$\boldsymbol{P} = \boldsymbol{P}' - \theta \boldsymbol{F}^{-t}. \tag{5.6}$$

For the case of locally drained conditions, we have $\delta \boldsymbol{P} = \delta \boldsymbol{P}'$ and thus, it is straight forward to show that the Eulerian acoustic tensor takes the classical form [29, 74]

$$A_{ik} \equiv A_{ik}^{d} = n_j a_{ijkl}^{\text{ep}} n_l \tag{5.7}$$

where a_{ijkl}^{ep} are the components of the total tangent operator defined in equation (4.37). Similarly, for the locally undrained case, we have $\boldsymbol{q} = \boldsymbol{0}$ point-wise, and consequently the equation of balance of mass (2.14) reduces to

$$\dot{\vartheta} = - \left(J \frac{K_{\text{f}}}{\phi^{\text{f}}} - \vartheta \right) \nabla^{\boldsymbol{x}} \cdot \boldsymbol{v}. \tag{5.8}$$

Taking the time derivative of $\boldsymbol{P}$ and utilizing equation (5.6), results in the undrained rate equation

$$\delta \boldsymbol{P} = \underbrace{\left[\mathbf{A}^{\text{ep}} + \left(J \frac{K_{\text{f}}}{\phi^{\text{f}}} - \theta \right) \boldsymbol{F}^{-t} \otimes \boldsymbol{F}^{-t} + \theta \boldsymbol{F}^{-t} \ominus \boldsymbol{F}^{-1} \right]}_{\overline{\mathbf{A}}^{\text{ep}}} : \delta \boldsymbol{F}, \tag{5.9}$$

where $\mathbf{A}^{\mathrm{ep}}$ and $\overline{\mathbf{A}}^{\mathrm{ep}}$ are the drained and undrained first elastoplastic tangent operators, respectively. Therefore, in this case we have

$$\boldsymbol{A} = \boldsymbol{A}^d + J\frac{K_{\mathrm{f}}}{\phi^{\mathrm{f}}}\boldsymbol{n} \otimes \boldsymbol{n}. \tag{5.10}$$

We note that the undrained acoustic tensor consists of the drained acoustic tensor plus a volumetric contribution emanating from the compressibility of the fluid phase. The expression for the acoustic tensor derived above is very similar to that obtained by Borja in [45] for the case of infinitesimal deformations.

Remark 5. The spectral search algorithm proposed by the authors in [29] is utilized in the next section to search for the onset of strain localization under both locally drained and locally undrained conditions utilizing suitable expressions for the acoustic tensor as obtained above.

6 Numerical simulations

In this section, several globally undrained plane strain compression test are performed. Macroscopically dense and loose samples of sand with and without inhomogeneities at the meso-scale are sheared to failure, whenever possible. The objective of these boundary-value problems is to study the effect of meso-scale inhomogeneities in the porosity on the stability and flow characteristics of sand specimens. It will be shown that the inhomogeneities, even though small, have a profound impact on the macroscopic behavior of the samples. Furthermore, it is shown that the constitutive model used to describe the effective stress for the underlying sand specimens captures some of the main features observed in sand specimens tested in the laboratory.

The material parameters utilized in the simulations are summarized in Tables 1 and 2. We refer the reader to Section 3 for details regarding the material parameters and their significance.

Symbol	Value	Parameter
$\widetilde{\kappa}$	0.03	compressibility
α_0	0	coupling coefficient
μ_0	2000 kPa	shear modulus
p_0	-99 kPa	reference pressure
$\epsilon_{\mathrm{v}0}^{\mathrm{e}}$	0	reference strain

Table 1: Summary of hyperelastic material parameters for plane strain compression problems.

Symbol	Value	Parameter
$\widetilde{\lambda}$	0.04	compressibility
M	1.2	critical state parameter
v_{c0}	1.8	reference specific volume
N	0.4	for yield function
$\overline{N}$	0.2	for plastic potential
ϱ	0.78	ellipticity
h	280/70	hardening coefficient for dense/loose samples

Table 2: Summary of plastic material parameters for plane strain compression problems.

6.1 Plane strain compression in globally undrained dense sands

In this subsection, we present the results obtained from performing globally undrained plane strain compression simulations on both inhomogeneous and homogeneous samples of dense sand. The inhomogeneous sample is constructed by prescribing a randomly generated specific volume field, which displays a higher horizontal than vertical correlation. The inhomogeneous sample is shown in Figure 4 where the initial specific volume field is superimposed on the undeformed finite element mesh. The sample is 5 cm wide and 10 cm tall and has been discretized using a mesh composed of 200 $Q9P4$ isoparametric elements [nine displacement nodes plus four (continuous) pressure nodes]. This kind of finite element has been shown to satisfy the Babuška-Brezzi stability condition and hence avoid stability problems associated with consolidation of porous media (see end of Section 4 for discussion on stability). The mean specific volume for the sample is 1.572, making the sample dense macroscopically. However, some pockets are relatively loose with specific volume as high as 1.64. The range in the specific volume for the dense sample is 1.54–1.64.

The boundary conditions for the numerical experiments are as follows. The top and bottom faces of the sample are supported on rollers (Dirichlet BCs) with the bottom left
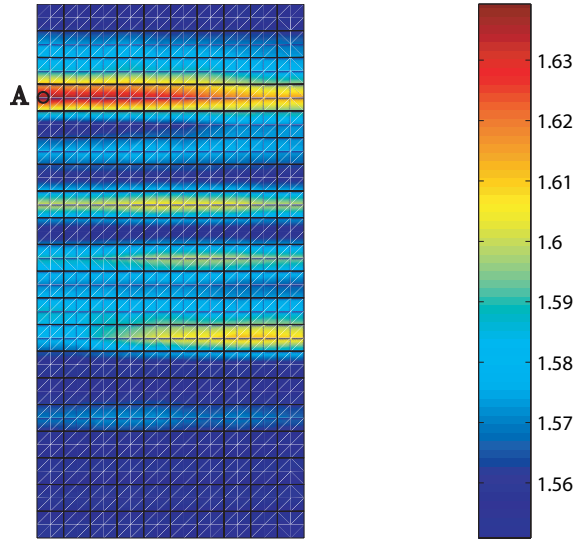
Figure 4: Initial specific volume for dense sand specimen superimposed on undeformed finite element mesh.

corner fixed with a pin for stability. The bottom face is constrained from displacing in the vertical direction, whereas the top face is given a vertical displacement responsible for compacting the sample in the axial direction. At the same time, the lateral faces are confined with an initial pressure of 100 kPa (Newman BCs) to simulate the confining pressure in a plane strain device. As for the boundary conditions associated with the flow equations, all faces of the sample are no-flow boundaries (Dirichlet BCs), provoking a globally undrained condition (although the permeability is finite locally and so there is a locally drained condition). This condition is equivalent to having an impermeable membrane surrounding the specimen, which is typically used in undrained compression tests in the laboratory. The testing conditions favor homogeneous deformations in the absence of material inhomogeneities and gravity effects.

The inhomogeneous sample of dense sand is loaded monotonically until failure. Figure 5(a) shows a plot of the determinant for the *drained* acoustic tensor at a deformed state after 5% nominal axial deformation. Also, the figure shows the contour of deviatoric strains at 5% axial strain with superimposed relative fluid flow vectors q in subfigure (b). The instant in time is selected so as to show a fully developed deformation band and to underscore the need for a finite deformation formulation. The developed deformation band allows for several interesting observations. It can be seen that the vanishing of the determinant for the drained acoustic
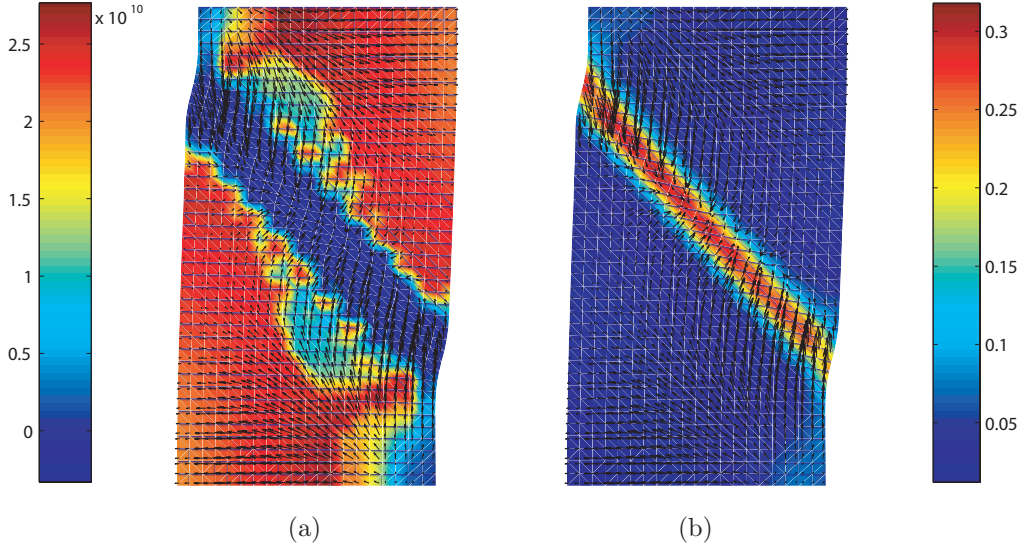
Figure 5: (a) Contour of the determinant function for the drained acoustic tensor at a nominal axial strain of 5% and (b) deviatoric strains in contour with superimposed relative flow vectors q at 5% axial strain for dense sand sample.

tensor $\boldsymbol{A}^d$ correlates very well with areas of intense localized deviatoric strains. Furthermore, the flow vectors q superimposed on both the contour for the determinant function and the contour for the deviatoric strain clearly show a strong influence of the deformation band on the flow characteristics in the sample. In fact, in this particular case, the deformation pattern appears to be 'attracting' the flow into the deformation band and away from the rest of the sample. This suggests a mostly dilative behavior of the sand within the deformation band, which will certainly tend to attract fluid flow.

The dilative behavior of the sand specimen can be clearly observed in Figure 6(a) where the contour for the volumetric strains is plotted against the deformed finite element mesh at an axial strain of 5%. Distinct areas of dilative (positive) volumetric response can be identified along the developed deformation band. This behavior is consistent with the signature behavior of relatively dense sands in the laboratory, which mostly tend to dilate during shear deformation [33, 75]. This dilative response has been also reproduced by plasticity models such as Drucker-Prager, which account for plastic dilation [10, 12] . This important feature is captured by the model developed herein by including meso-scale information about the porosity (and hence relative density) in the hardening law via the state parameter ψ_i. Be-

35
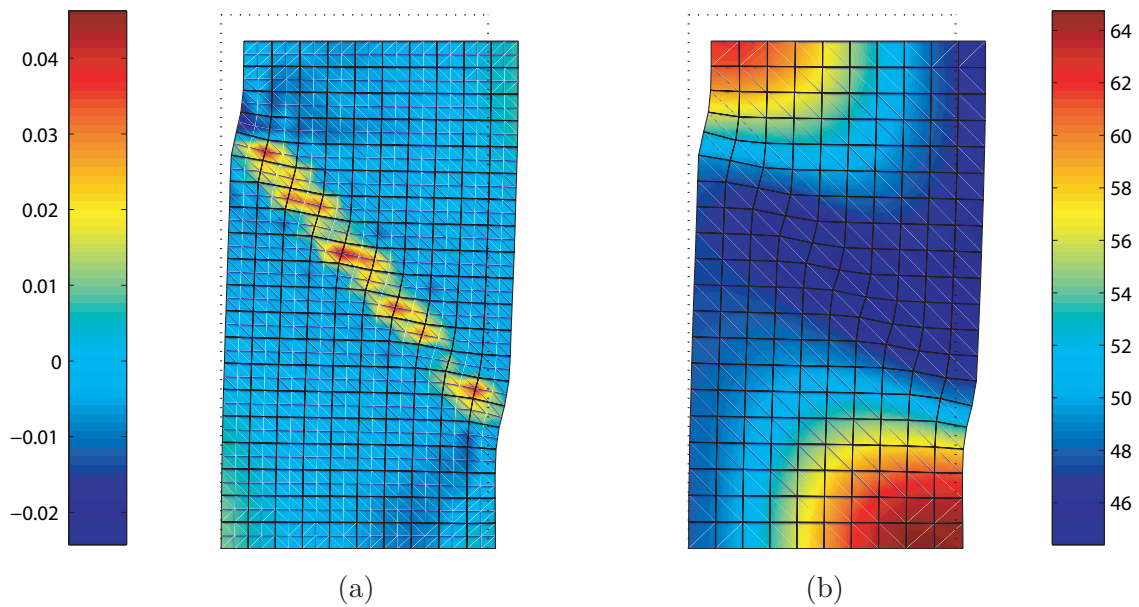
Figure 6: (a) Volumetric strain contour superimposed on deformed finite element mesh at 5% axial strain and (b) contour of Cauchy fluid pressure p on deformed sample at 5% axial strain (in kPa) for dense sand sample. Dotted lines delineate undeformed configuration.

cause of the coupling effect between the response of the porous medium and the fluid flow, Figure 6(b) shows distinct areas of low Cauchy fluid pressures corresponding to those where the volumetric response is dilative. In fact, it is obvious from the figure that strong gradients in the fluid pressure are generated and are consistent with the deformation pattern of the sample and are responsible for the amount and direction of fluid flow. It should be noted at this point that because of the small dimensions of the sample, gravitational effects do not play a major role and hence there is not much meaning in distinguishing 'excess' pore fluid pressure from total pore fluid pressure.

At this point, it is clear that the deformation pattern is strongly coupled with the fluid flow, but it is not clear what the role of the meso-scale is in the overall stability of the undrained sample. To shed some light into this question, we compare the response of the inhomogeneous sand sample against its homogeneous counterpart. This type of analyses has been performed before in the context of *drained* or effective material response (e.g., see [29, 30] for analyses on 'dry' samples of dense sand). In these previous studies, it was found that the meso-scale is responsible for triggering instabilities at the specimen scale, reducing the load carrying
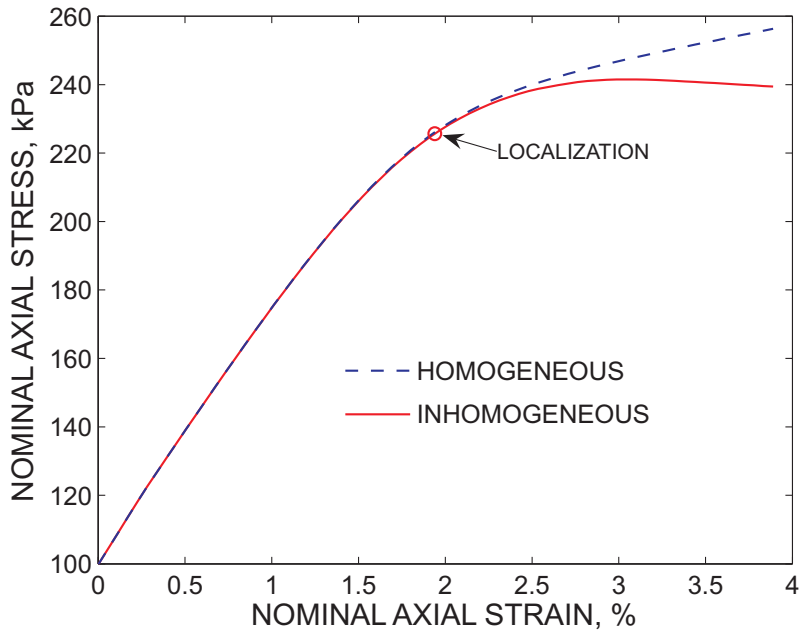
Figure 7: Force-displacement curve for inhomogeneous and homogeneous samples of dense sand.

capacity of the sample of dense sand. The same type of analysis is performed here with very similar results. The force-displacement curves for both inhomogeneous and homogeneous samples of dense sand are plotted in Figure 7. In this figure, the reactive stresses at the top face of the samples are plotted against the nominal axial strain. The homogeneous sample is constructed by imposing a constant value of initial specific volume at 1.572 (the mean value of the distribution shown in Figure 4). The load-displacement responses are superimposed on each other for the first 2% axial strain, at which point the inhomogeneous sample bifurcates (both drained and undrained acoustic tensors loose positive definiteness at about 1.9% axial strain). The homogeneous sample does not localize and in fact continues to harden until the end of the simulation at 4% axial strain. On the other hand, after localization is detected in the inhomogeneous sample, the response is characterized by softening and the sample does not recover its load carrying capacity.

Localization above is defined as the first time either the drained or undrained acoustic tensor loses positive definiteness at any (Gauss) point in the sample. The point where the sample localized for the first time is shown in Figure 4 and referred to as point A. The
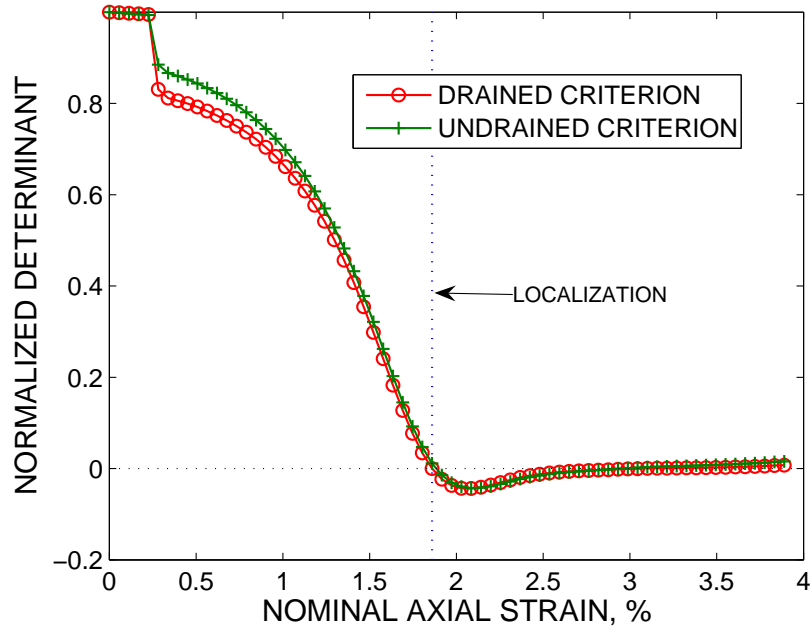
Figure 8: Normalized determinant functions at point A for dense sand sample.

determinant functions for both drained and locally undrained acoustic tensors at point A are plotted in Figure 8. Localization occurred around 1.9% nominal axial strain when both determinants for the drained and undrained acoustic tensor went negative for the first time. In this particular case, both localization criteria coincided, but in cases when the point in question was below the critical state line, the drained localization criterion superseded the undrained criterion. In this particular simulation, we never observed the determinant of the undrained acoustic tensor vanishing before that of the drained acoustic tensor.

Once localization occurs at point A, the modes of deformation tend to change considerably at that location. As expected, deviatoric deformations are magnified once localization is detected. The volumetric and deviatoric strain invariants are plotted in Figure 9 where it is easily seen that after 1.9% axial strain, the slope of the deviatoric strain curve is about five times steeper than before localization is detected. Also, the point in question seems to compact very little initially, followed by significant dilation, which is consistent with the macroscopic behavior of dense sands. The volumetric behavior of point A can be further observed from Figure 10 where the specific volume at that point is plotted against the effective pressure and
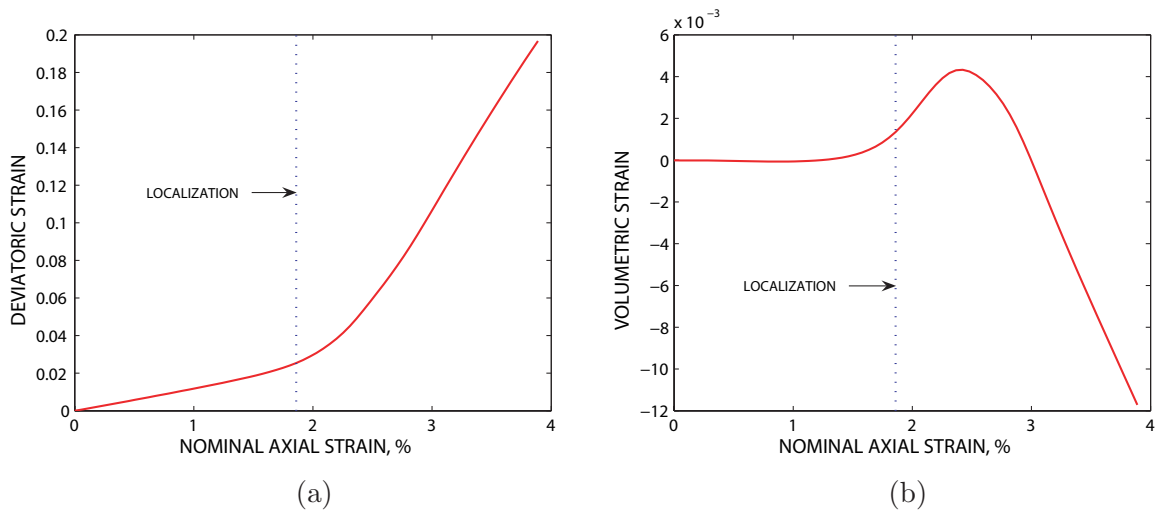
Figure 9: (a) Deviatoric strain invariant at Gauss point A for sample of dense sand (b) volumetric strain invariant at Gauss point A for sample of dense sand.

the CSL for the material is plotted for reference. It is interesting to note that even though point A lies above the critical state line, its volumetric behavior is closer to that of a drained point below the CSL. This is because the rest of the sample is behaving macroscopically as a dense sand and the coupling between the solid matrix and the fluid flow is really what governs deformation. The matrix at point A may 'want' to contract, but the fact that point A is more permeable that some other parts of the sample makes it easier for the fluid to flow into point A and hence force it to dilate. This last observation shows that the saturated behavior of a globally undrained sample could be sharply distinct to that of a perfectly drained one.

6.2 Plane strain compression in globally undrained loose sands

To obtain a somewhat complete picture of the behavior of saturated granular materials under shear deformations, globally undrained compression tests are performed on samples of macroscopically loose sands. In this set of tests, we compare the response of an inhomogeneous sample of sand against its homogeneous counterpart. As in the previous subsection, the initial inhomogeneity is furnished by the initial distribution of specific volume, which follows a pattern identical to that shown in Figure 4 above. The only difference here is the range and mean of the distribution in order to reflect a macroscopically loose sample of sand. The
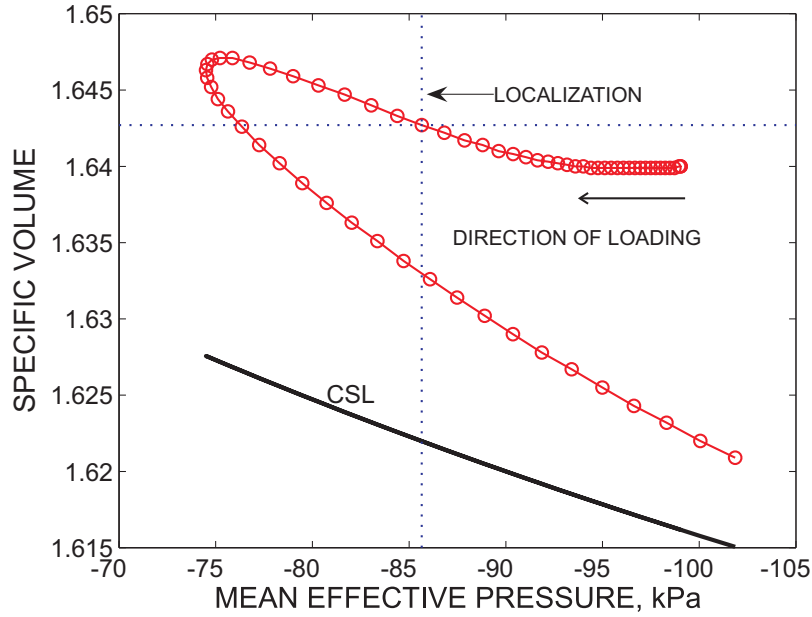
Figure 10: Specific volume plot as a function of effective pressure at point A for dense sand sample

initial range of specific volume for the loose sample is depicted in Figure 11 and goes from 1.62 to 1.66. This particular range is much narrower than that chosen in the previous set of simulations, the sample appears to be more homogeneous than the dense sand sample. The average specific volume for the sample of loose sand is 1.62 (cf. with that for the dense sand sample at 1.572). This average value of specific volume puts the sample above the CSL on average and hence we expect the behavior of the structure to be macroscopically similar to a homogeneous sample of loose sand. As for the rest of the material parameters, they are almost identical to those in the previous subsection and are summarized in Tables 1 and 2. The only difference in the material parameters between the dense sand samples and the loose ones is the hardening coefficient h, which is 280 in the case of the dense sands and 70 for the loose sands. This reflects the fact that relatively loose sands show 'flatter' force-displacement curves.

The 5×10 cm sample is discretized using the same mesh as the dense sand samples and the imposed boundary conditions are also identical. Hence, any difference in the behavior
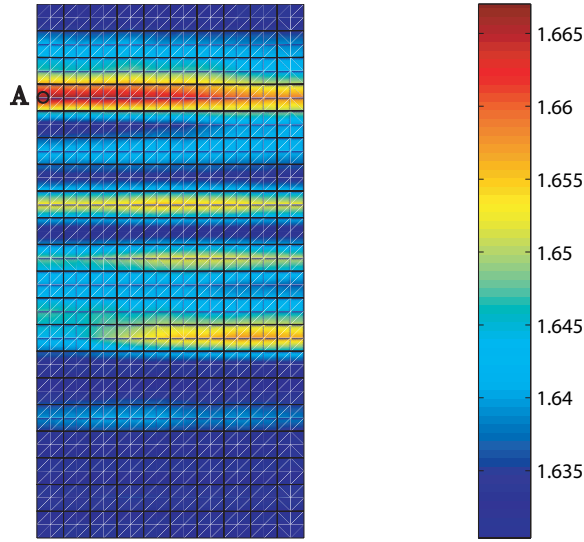
Figure 11: Initial specific volume for loose sand specimen superimposed on undeformed finite element mesh.

of the structure is due to the different phenomenological behavior implied by the underlying effective stress constitutive model and triggered by the difference in relative densities. This is due to the fact that the phenomenological model can realistically capture the difference in behavior of sand samples at different relative densities.

Similar to the dense sand sample, the inhomogeneous sample of loose sand is loaded monotonically by prescribing a uniform vertical displacement at the top face of the sample. Figure 12 shows a plot of the determinant of the *undrained* acoustic tensor and the deviatoric strain invariant for the loose sand sample at 5% axial strain. The relative flow vectors $\boldsymbol{q}$ are superimposed on the aforementioned contours to give a relative sense of the interaction between the deformation and flow patterns. Once again, the instant in time is chosen such that the deformation band is fully developed. As in the case of the dense sand sample, the localization criterion for the undrained acoustic tensor $\boldsymbol{A}$ correlates very well with high concentrations of deviatoric strains in the sample. In fact, the profile for the determinant of the drained acoustic tensor $\boldsymbol{A}^d$ looks similar with a different order of magnitude throughout. The deformation pattern again influences the flow characteristics in the sample but with an opposite effect to that observed in the dense sample. For the case of loose sand deforming under globally undrained conditions, the incipient shear band appears to be 'repelling' fluid
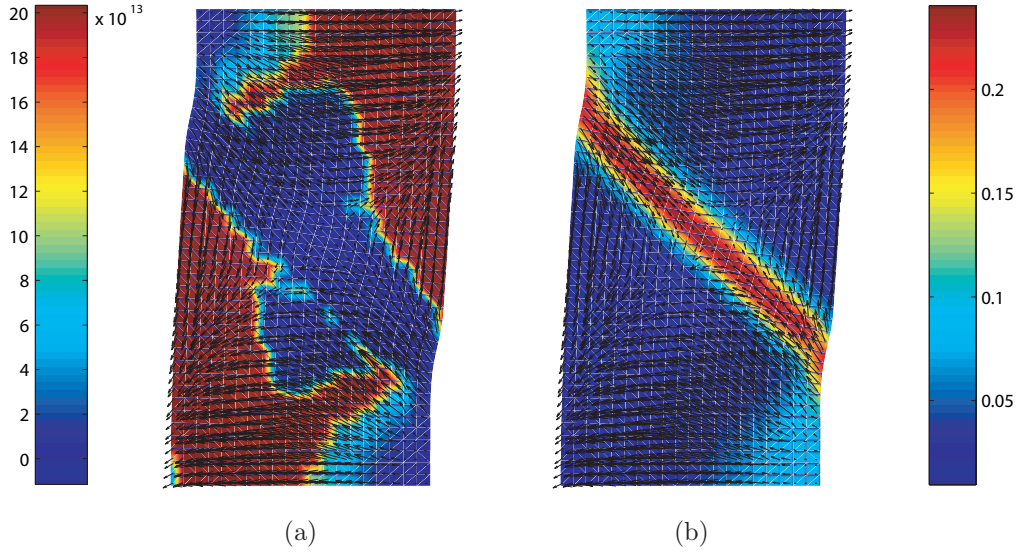
Figure 12: (a) Contour of the determinant function for the undrained acoustic tensor at a nominal axial strain of 5% and (b) deviatoric strains in contour with superimposed relative flow vectors q at 5% axial strain for loose sand sample.

flow. This deformation-diffusion behavior suggests a compactive behavior within the shear band compared to a relatively less compressive and perhaps even dilative deformation pattern elsewhere in the sample. Another contrasting feature is the fact that the deformation band is initially (at lower values of axial strain) less pronounced and less localized and looks more diffuse than that for the dense sample, which is again consistent with the behavior of relatively loose sands which tend to fail in a more diffuse mode in the laboratory. These seem to be a novel results since, as far as we know, no results showing compactive shear bands repelling fluid flow have been reported in the literature (e.g. see works by Armero [10] and Larsson and Larsson [12] who only report *dilative* shear bands).

The suggested compactive behavior within the deformation band is truly appreciated when one plots the volumetric strain invariant at 5% axial strain. Figure 13(a) shows such deformation contour superimposed on the deformed finite element mesh. There are well-defined pockets of compactive behavior on what can be defined as the ends of the deformation band. The rest of the band is not as compactive (in fact the center is slightly dilating) as the ends, but the upper-right and lower-left corners are much more dilative in comparison to the band. This is the reason why the fluid pressure contour shown in 13(b) looks like a saddle.
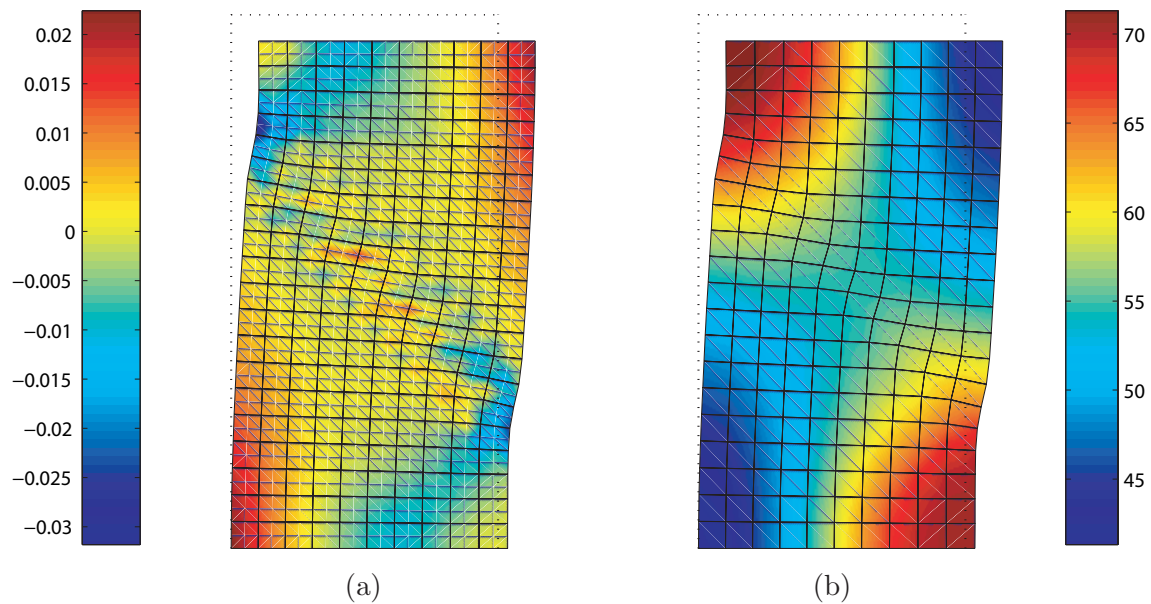
Figure 13: (a) Volumetric strain contour superimposed on deformed finite element mesh at 5% axial strain and (b) contour of Cauchy fluid pressure p on deformed sample at 5% axial strain (in kPa) for loose sand sample. Dotted lines delineate undeformed configuration.

There is a relative low at the center of the band (and the specimen) but there are maxima at the ends of the deformation band. The dilative pockets described above constitute regions where the Cauchy fluid pressure p is at a minimum in the sample. This explains the direction of the relative flow, which tends to go away from the ends of the deformation band, towards the center of the band and in general away from the band (see Figure 12 above). This pressure and flow pattern is clearly different from that observed in the sample of dense sand and is consistent with the behavior of an undrained sample of relatively loose sand.

The effect of the inhomogeneities in the porosity field at the meso-scale can be seen by comparing the force-displacement curve for the inhomogeneous sample against that of the homogeneous sample. Figure 14 shows a plot of the nominal axial stress at the top face for both inhomogeneous and homogeneous samples of loose sand. The curves are clearly identical up to about 2.4% axial strain point at which the inhomogeneous sample localizes and subsequently softens. The homogeneous sample did not localize by any criterion and did not show any signs of softening up to 4% axial strain. The fact that the curves coincide up to the point of bifurcation suggests that the effect of the meso-scale inhomogeneity is minimal early

43
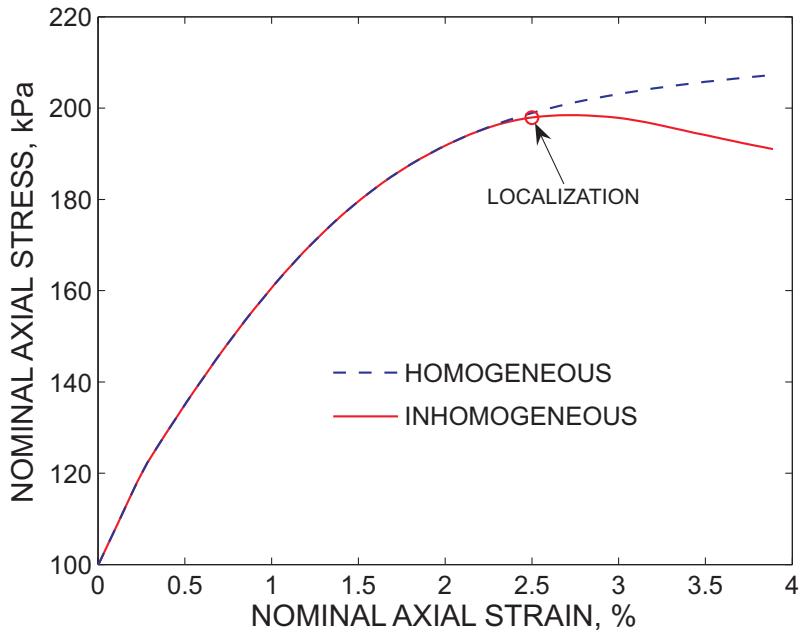
Figure 14: Force-displacement curve for inhomogeneous and homogeneous samples of loose sand.

in the deformation-diffusion process. However, it is clear that the inhomogeneities ultimately alter the load-carrying capacity of the inhomogeneous sample, which is macroscopically softer than its homogeneous counterpart. Also note the flatter slope in the force-displacement curves obtained for the loose sample than those for the dense sample; a direct effect of the relative density and hardening coefficient.

The localization point at 2.4% axial strain is defined by the vanishing of the determinant of both drained and undrained acoustic tensors at point A, which is depicted in Figure 11. Both localization criteria are met at the same time at point A and hence there is no room for ambiguity when one speaks of loss of positive definiteness of the acoustic tensor. It is interesting to note that localization occurs first at the same point in both dense and loose samples. This might be due to the fact that this point is relatively looser in both specimens and hence tends to fail first in both instances. Figure 15 shows a plot of the normalized determinant for both the drained and locally undrained acoustic tensors. It is observed that both determinants vanish at around 2.4% axial strain. In this simulation, all points that lost positive definiteness of the acoustic tensor did so for the drained and undrained acoustic
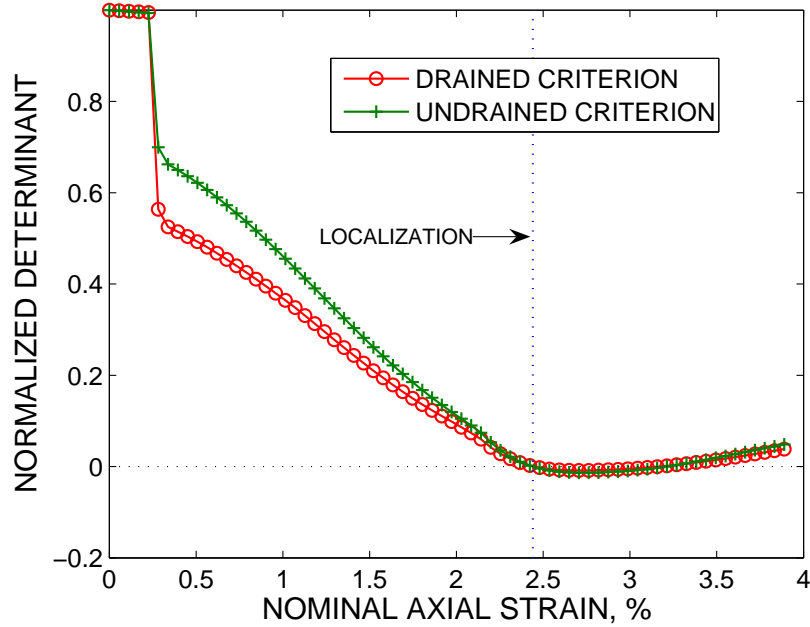
Figure 15: Normalized determinant functions at point A for loose sand sample.

tensors at the same time. Comparison with the dense sand simulation shows that localization was attained at a later time, which suggests a more ductile behavior associated with the loose sand sample.

It is interesting to observe the modes of deformations at point A in the sample before and after localization is attained. As in the dense sand sample, point A exhibits a steepening in the slope of the deviatoric strain after localization, which is shown in Figure 16(a). In fact, the sample exhibits three times more deviatoric deformation in the last 1.6% axial strain than in the first 2.4% axial strain. Also, point A remains basically incompressible up to the onset of localization. Figure 16(b) shows the volumetric strain invariant versus axial strain, where it is observed that point A did not change in volume until it reached localization, after which point it compacted quite a bit. In this case, which can be contrasted to the case of the dense sample of sand, point A behaves more as a typical 'drained' point after localization: experiencing volume loss, which leads to an area of high pressure because the fluid cannot escape fast enough. Figure 17 shows the relation between specific volume and the mean Kirchhoff effective pressure. The specific volume is essentially constant up to the

45
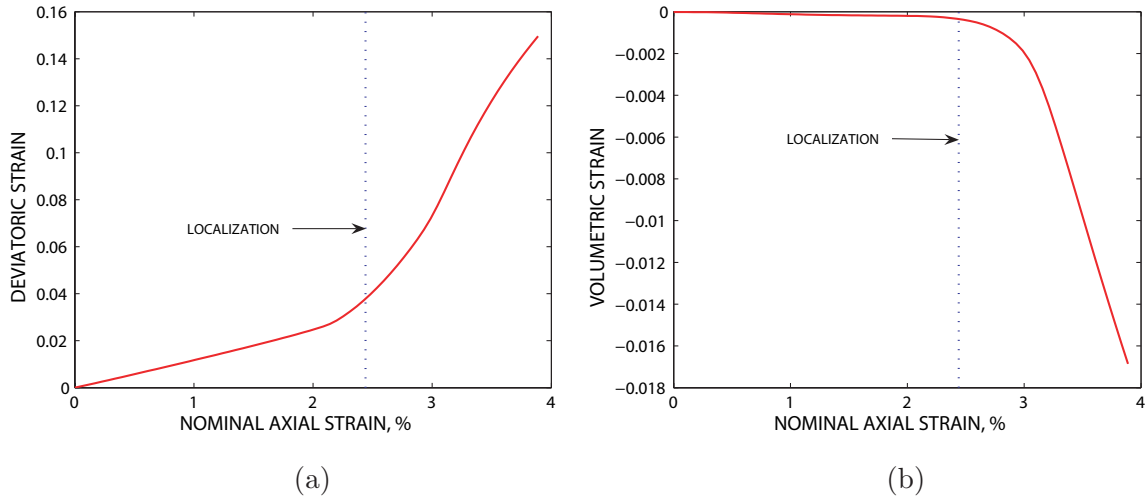
Figure 16: (a) Deviatoric strain invariant at Gauss point A for sample of loose sand (b) volumetric strain invariant at Gauss point A for sample of loose sand.

onset of localization and subsequently the state is attracted towards the CSL. Once again, the behavior at point A is of course affected by the surrounding area in the sample and also, and perhaps more importantly, by the coupling imposed by the balance laws.

Finally, Figure 18 shows the convergence profile at various stages in the loading protocol for the plane strain compression test on the inhomogeneous sample of loose sand. Consistent linearization performed in the proposed finite element procedure, combined with the fact that the effective stress constitutive model features a consistent tangent operator available in closed form [29], leads to an overall rate of convergence that enjoys the optimal quadratic rate associated with the full Newton-Raphson scheme. Furthermore, the fact that finite elements satisfying the Babuška-Brezzi stability condition are utilized translates into solutions free of spurious oscillations in the fluid pressure associated with instabilities near initial time when the sample behaves as an incompressible solid [68, 70].

Remark 6. It is important to note that the finite element solutions presented above do suffer from mild pathological mesh dependence once the onset of localization has been detected. It has been show by Zhang and Schrefler [76] that even though the fluid flow equation introduces a length scale via the permeability coefficient, it might not be enough if the effective stress equations are not further regularized by, say, adding a viscous term. However, the conclusions
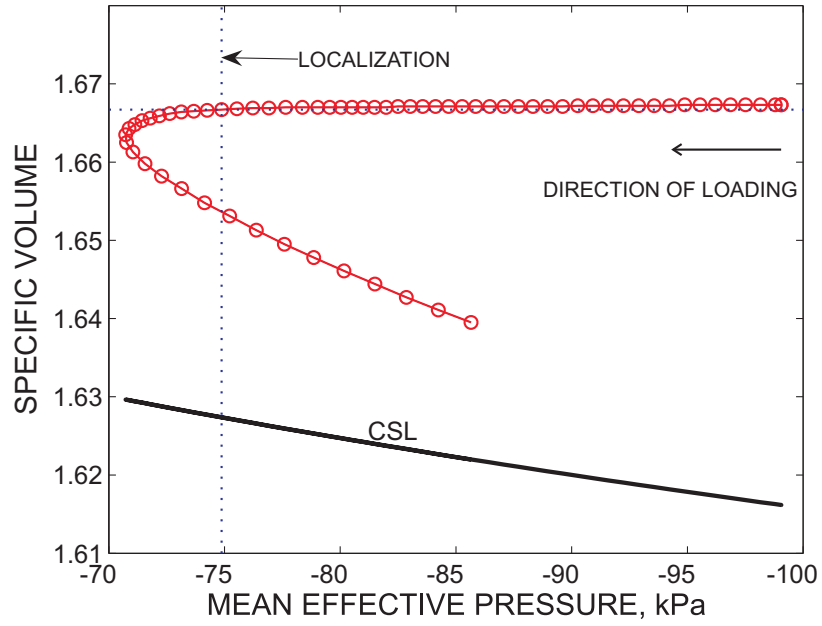
Figure 17: Specific volume plot as a function of effective pressure at point A for loose sand sample
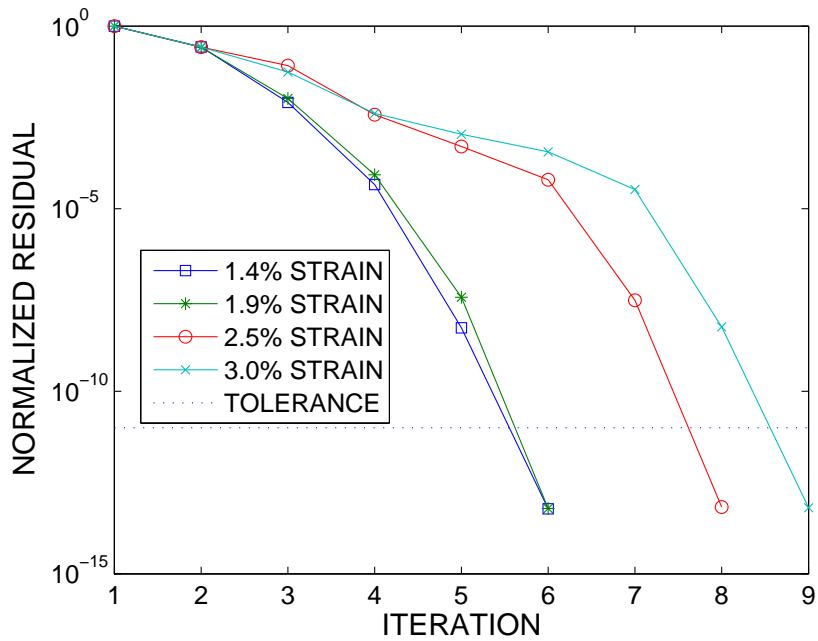

Figure 18: Convergence profile at various values of axial strain for plane strain compression test on sample of loose sand.

reached above are qualitative and should not be affected by this detail.

To illustrate this 'mild' dependence, we perform a simple mesh sensitivity study. For simplicity, we solve same boundary value problem presented above in Section 6.1. Consider the same homogeneous sample with specific volume $v = 1.572$ but with an arbitrary 'weak' region (i.e., $v = 1.6$) in the specimen as illustrated in Figure 19. Two meshes are analyzed: one consisting of 50 $Q9P4$ elements and another one consisting of 200 such elements. The results of the undrained compression tests are summarized in Figures 20 and 21. Figure 20 shows the force displacement curves for the 50 and 200 element mesh compared against the perfectly homogeneous response (i.e., $v = 1.572$ throughout). It is shown that the perturbed samples are less stiff than the homogeneous sample and that the responses of the two inhomogeneous samples are identical up to 3% axial strain, corresponding to a level of strain passed the drained localization criterion. In fact both inhomogeneous samples detect the onset of drained localization simultaneously, as expected. By the time undrained localization is detected in the fine mesh sample, the force displacement curves are starting to diverge.

Figure 21 shows the deviatoric strains with superimposed relative flow vectors on both finite element meshes. It is clear that the apparent width of the shear band is a function of the element size; the width of the shear band decreases proportional to the element size. However, the pattern of deformation and the direction of flow is identical in both samples. Both samples develop dilative shear bands that tend to attract fluid flow. Hence, we say mesh dependence is 'mild' as both meshes display the same overall mechanical behavior: both predict softer responses, identical onset of drained localization, and appearance of dilative shear bands.

7 Conclusion

We have presented a finite element model for the simulation of saturated porous media exhibiting meso-scale inhomogeneities in the porosity field. The continuum balance laws have been derived and utilized within a finite element framework from which the basic unknowns: solid displacements and Cauchy pore fluid pressures have been resolved in a $\boldsymbol{u} - p$ mixed finite element scheme. The scheme features stable solutions with optimum rates of convergence.
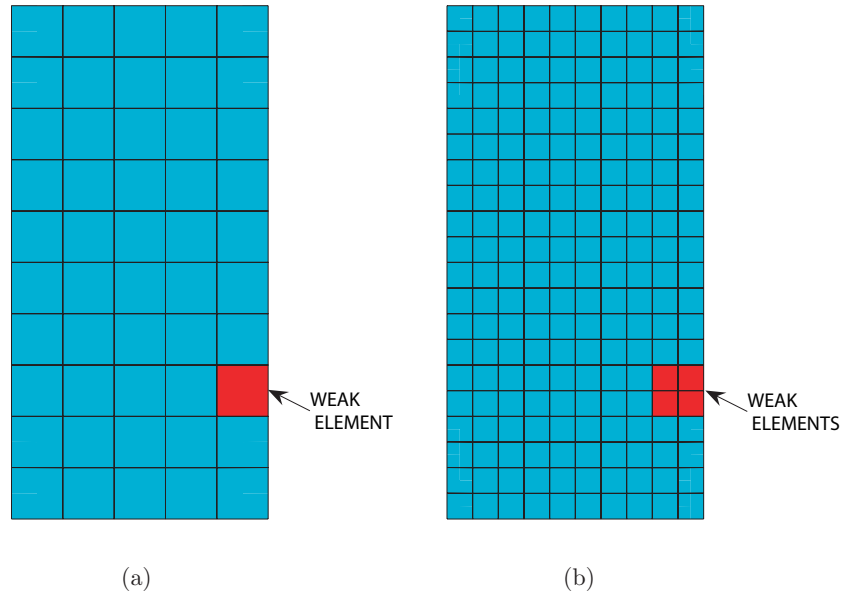
48

(a)   (b)

Figure 19: Perturbed samples of dense sand with otherwise homogeneous specific volume $v = 1.572$. (a) Mesh composed of 50 $Q9P4$ elements and (b) mesh composed of 200 $Q9P4$.
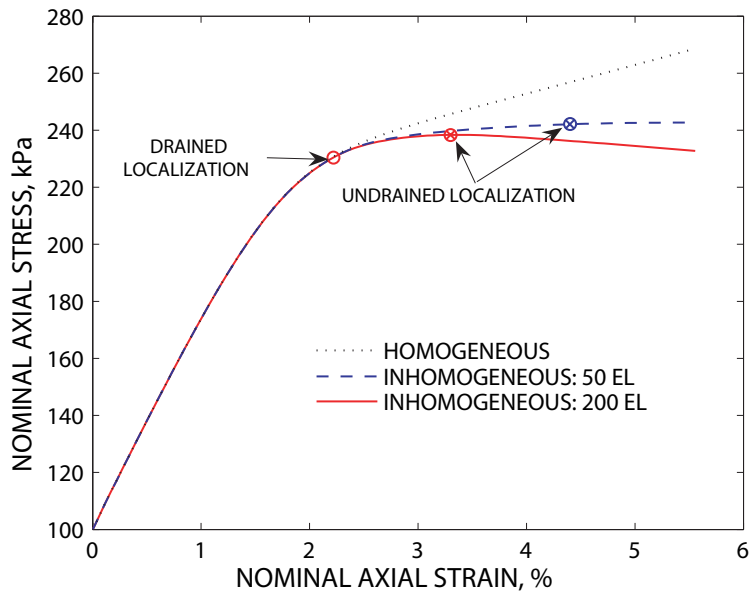

Figure 20: Force displacement curves comparing perfectly homogeneous response to that of perturbed samples
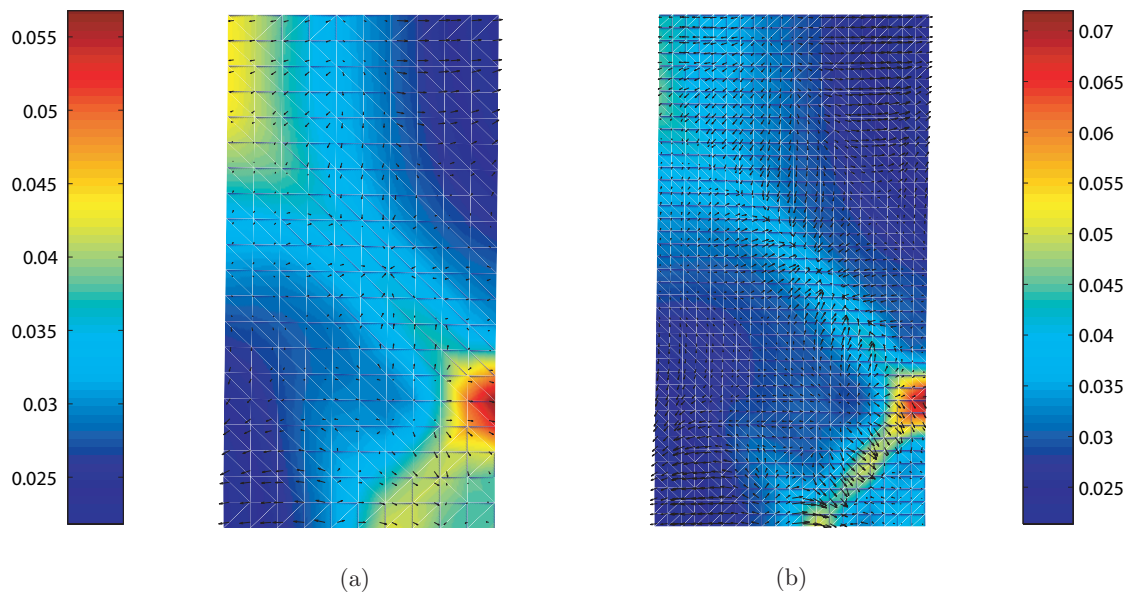
Figure 21: Deviatoric strains in contours with superimposed relative flow vectors $\boldsymbol{q}$ at 3% axial strain for (a) 50 element mesh and (b) 200 element mesh

Representative numerical examples dealing with plane strain compression of undrained samples of dense and loose sands have been presented to underscore the importance of meso-scale inhomogeneities on the stability and flow characteristics through a deforming sand specimen. We have shown that behavior of saturated granular media is more complex than that inferred from macroscopic observations and that even small imperfections at a scale smaller than specimen size can trigger global failure and influence the amount and direction of flow. Furthermore, the behavior of relatively dense and loose samples differ substantially as the volumetric behavior of the solid matrix is coupled with the fluid flow, hence affecting the effective pressures, which govern strength in geomaterials. These last observations are unique to this study in which porosity has been coupled with the hydraulic conductivity and effective stress behavior of the underlying granular media, thereby capturing both compactive and dilative modes of deformation banding.

Acknowledgements

Appendix A

Equation (4.42) can be rewritten in indicial notation as

$$\delta g_1 = c_{iA} \int_{\Omega_0} \left[N_{A,j} \left(a_{ijkl}^{\text{ep}} + Jp \left(\delta_{il}\delta_{jk} - \delta_{ij}\delta_{kl} \right) \right) N_{B,l} \delta d_{Bk} - J N_{A,i} \overline{N}_B \delta p_B \right] \mathrm{d}\Omega_0, \qquad \text{(A.1)}$$

following the notations in [41] (cf. equations (4.49) and (4.51)),

$$u_i \approx \sum_{A \in \eta - \eta_d} N_A d_{iA} + \sum_{A \in \eta_d} N_A^\xi \xi_A \qquad \text{(A.2)}$$

$$p \approx \sum_{A \in \overline{\eta} - \eta_p} \overline{N}_A p_A + \sum_{A \in \eta_p} N_A^\zeta \zeta_A \qquad \text{(A.3)}$$

$$\eta_i \approx \sum_{A \in \eta - \eta_d} N_A c_{iA} \qquad \text{(A.4)}$$

$$\psi \approx \sum_{A \in \overline{\eta} - \eta_p} \overline{N}_A \overline{c}_A \qquad \text{(A.5)}$$

where η and $\overline{\eta}$ denote the set of global node numbers for the displacement and pressure, respectively. Similarly, we let η_d and η_p be the nodes at which the displacements and pressures are prescribed, hence $\eta - \eta_d$ and $\overline{\eta} - \eta_p$ represent the active sets for the displacement and pressure, respectively. By the same token,

$$\delta g_2 = -c_{iA} \int_{\Omega_0} J N_A \gamma_{\text{f}i} \left[N_{B,j} \delta d_{jB} + \frac{\phi^{\text{f}}}{K_{\text{f}}} \overline{N}_B \delta p_B \right] \mathrm{d}\Omega_0. \qquad \text{(A.6)}$$

The linearized equations pertaining to the balance of mass equations can also be rewritten

in indicial notation i.e.,

$$\delta h_1^{\Delta t} = \overline{c}_A \int_{\Omega_0} J\overline{N}_A \rho_f \left[N_{B,j} \delta d_{jB} + \frac{\phi^f}{K_f} \overline{N}_B \delta p_B \right] d\Omega_0, \tag{A.7}$$

and

$$\begin{aligned}
\delta h_2^{\Delta t} &= \frac{\alpha \Delta t}{g} \overline{c}_A \int_{\Omega_0} Jk_{ij} \left[\overline{N}_{A,i} N_{B,k} \delta d_{kB} - \overline{N}_{A,k} N_{B,i} \delta d_{kB} \right] (p_{,j} - \gamma_{fj}) \, d\Omega_0 \\
&+ \frac{\alpha \Delta t}{g} \overline{c}_A \int_{\Omega_0} \frac{J}{\mu} \overline{N}_{A,i} \delta_{ij} k' \gamma_f \left(1 - \phi^f \right) N_{B,k} \delta d_{kB} (p_{,j} - \gamma_{fj}) \, d\Omega_0 \\
&+ \frac{\alpha \Delta t}{g} \overline{c}_A \int_{\Omega_0} J\overline{N}_{A,i} \frac{k_{ij}}{K_f} \overline{N}_B \delta p_B (p_{,j} - \gamma_{fj}) \, d\Omega_0 \\
&+ \frac{\alpha \Delta t}{g} \overline{c}_A \int_{\Omega_0} J\overline{N}_{A,i} k_{ij} \left[\overline{N}_{B,j} \delta p_B - \frac{\gamma_{fj}}{K_f} \overline{N}_B \delta p_B - p_{,k} N_{B,j} \delta d_{kB} \right] d\Omega_0. \tag{A.8}
\end{aligned}$$

From this point forward we adopt Voigt notation and hence, a fourth-order tensor $\boldsymbol{\alpha}$ is mapped into a 9×9 array i.e.,

$$\boldsymbol{\alpha} = \begin{bmatrix} [\alpha_{iikk}] & [\alpha_{ii(kl)}] & [\alpha_{ii[kl]}] \\ [\alpha_{(ij)kk}] & [\alpha_{(ij)(kl)}] & [\alpha_{(ij)[kl]}] \\ [\alpha_{[ij]kk}] & [\alpha_{[ij](kl)}] & [\alpha_{[ij][kl]}] \end{bmatrix} \qquad \text{(no sum)} \tag{A.9}$$

where $i, j, k, l = 1, 2, 3$, and $i \neq j$ and $k \neq l$. Also, each submatrix in square brackets represents a 3×3 array. For example,

$$\left[\alpha_{(ij)[kl]} \right] = \begin{bmatrix} \alpha_{(12)[12]} & \alpha_{(12)[23]} & \alpha_{(12)[31]} \\ \alpha_{(23)[12]} & \alpha_{(23)[23]} & \alpha_{(23)[31]} \\ \alpha_{(31)[12]} & \alpha_{(31)[23]} & \alpha_{(31)[31]} \end{bmatrix}, \tag{A.10}$$

where the parentheses signify a symmetric operator, whereas the square brackets signify a skew-symmetric operator. For example,

$$\alpha_{(12)[23]} = \frac{1}{4} \left(\alpha_{1223} - \alpha_{1232} + \alpha_{2123} - \alpha_{2132} \right). \tag{A.11}$$

52

Similarly, a second-order tensor $\nabla^{x}\boldsymbol{\eta}$ is mapped into a 9×1 vector i.e.,

$$\nabla^{x}\boldsymbol{\eta} = \left\{ \eta_{1,1}, \eta_{2,2}, \eta_{3,3}, 2\eta_{(1,2)}, 2\eta_{(2,3)}, 2\eta_{(3,1)}, 2\eta_{[1,2]}, 2\eta_{[2,3]}, 2\eta_{[3,1]} \right\}^{t} \tag{A.12}$$

such that the scalar product $\eta_{i,j}\alpha_{ijkl}\eta_{k,l} \equiv \nabla^{x}\boldsymbol{\eta}^{t}\boldsymbol{\alpha}\nabla^{x}\boldsymbol{\eta}$ is recovered. Also, given the finite element approximations in $(4.51)_{1,2}$ we have

$$\nabla^{x}\boldsymbol{\eta} = \boldsymbol{Bc} \tag{A.13}$$

$$\nabla^{x}\boldsymbol{\psi} = \boldsymbol{\Gamma}\overline{\boldsymbol{c}}, \tag{A.14}$$

where $\boldsymbol{B}$ is the usual strain-displacement matrix i.e., $\boldsymbol{B} = [\boldsymbol{B}_{1}, \boldsymbol{B}_{2}, \dots, \boldsymbol{B}_{nu}]$, and

$$\boldsymbol{B}_{A} = \begin{bmatrix} N_{A,1} & 0 & 0 \\ 0 & N_{A,2} & 0 \\ 0 & 0 & N_{A,3} \\ N_{A,2} & N_{A,1} & 0 \\ 0 & N_{A,3} & N_{A,2} \\ N_{A,3} & 0 & N_{A,1} \\ N_{A,2} & -N_{A,1} & 0 \\ 0 & N_{A,3} & -N_{A,2} \\ -N_{A,3} & 0 & N_{A,1} \end{bmatrix}. \tag{A.15}$$

By the same token, the matrix $\boldsymbol{\Gamma} = [\boldsymbol{\Gamma}_{1}, \boldsymbol{\Gamma}_{2}, \dots, \boldsymbol{\Gamma}_{np}]$. The components of $\boldsymbol{\Gamma}$ read

$$\boldsymbol{\Gamma}_{A} = \left\{ \overline{N}_{A,1}, \overline{N}_{A,2}, \overline{N}_{A,3} \right\}^{t}. \tag{A.16}$$

It is convenient at this point to introduce the following operators. Let $\boldsymbol{a}$ be a vector or

first-order tensor with components a_i with $i = 1, 2, 3$, then let

$$\epsilon\left(\boldsymbol{a}\right) = \begin{bmatrix} a_1 & 0 & 0 & \frac{1}{2}a_2 & 0 & \frac{1}{2}a_3 & \frac{1}{2}a_2 & 0 & -\frac{1}{2}a_3 \\ 0 & a_2 & 0 & \frac{1}{2}a_1 & \frac{1}{2}a_3 & 0 & -\frac{1}{2}a_1 & \frac{1}{2}a_3 & 0 \\ 0 & 0 & a_3 & 0 & \frac{1}{2}a_2 & \frac{1}{2}a_1 & 0 & -\frac{1}{2}a_2 & \frac{1}{2}a_1 \end{bmatrix}. \tag{A.17}$$

Similarly, let $\boldsymbol{\beta}$ be a third-order tensor with components β_{ijk} where $i, j, k = 1, 2, 3$, then

$$\boldsymbol{r}\left(\beta_{ijk}\right) = \begin{bmatrix} [\beta_{ikk}] & [\beta_{i(jk)}] & [\beta_{i[jk]}] \end{bmatrix} \qquad \text{(no sum)} \tag{A.18}$$

where $j \neq k$ within the 3×9 array. Each submatrix in square brackets represents a 3×3 array, for instance,

$$[\beta_{ikk}] = \begin{bmatrix} \beta_{111} & \beta_{122} & \beta_{133} \\ \beta_{211} & \beta_{222} & \beta_{233} \\ \beta_{311} & \beta_{322} & \beta_{333} \end{bmatrix} \tag{A.19}$$

Using the arrays and mappings presented above, we can write the matrix equation for the iterative Newton-Raphson scheme. The variational form for the equation of linear momentum implies

$$\boldsymbol{R}_g^k = \begin{bmatrix} \boldsymbol{K}_g & \boldsymbol{\Phi}_g \end{bmatrix}_k \left\{ \begin{array}{c} \delta\boldsymbol{d} \\ \delta\boldsymbol{p} \end{array} \right\}_{k+1}, \tag{A.20}$$

where

$$\boldsymbol{K}_g = \int_{\Omega_0} \left[\boldsymbol{B}^t \left(\boldsymbol{a}^{\text{ep}} + Jp \left(\boldsymbol{1} \ominus \boldsymbol{1} - \boldsymbol{1} \otimes \boldsymbol{1} \right) \right) \boldsymbol{B} - \boldsymbol{N}^t \boldsymbol{\gamma}_{\text{f}} J \boldsymbol{\delta}^t \boldsymbol{B} \right] \mathrm{d}\Omega_0 \tag{A.21}$$

$$\boldsymbol{\Phi}_g = -\int_{\Omega_0} J \left[\boldsymbol{B}^t \boldsymbol{\delta}\overline{\boldsymbol{N}} + \boldsymbol{N}^t \boldsymbol{\gamma}_{\text{f}} \frac{\phi^{\text{f}}}{K_{\text{f}}} \overline{\boldsymbol{N}} \right] \mathrm{d}\Omega_0, \tag{A.22}$$

with $\boldsymbol{\delta} = \{1, 1, 1, 0, 0, 0, 0, 0, 0\}^t$. Similarly, the variational form for the integrated (in time) equation of balance of mass implies

$$\boldsymbol{R}_h^k = \begin{bmatrix} \boldsymbol{K}_h + \alpha\Delta t\overline{\boldsymbol{K}}_h & \boldsymbol{\Phi}_h + \alpha\Delta t\overline{\boldsymbol{\Phi}}_h \end{bmatrix}_k \left\{ \begin{array}{c} \delta\boldsymbol{d} \\ \delta\boldsymbol{p} \end{array} \right\}_{k+1}, \tag{A.23}$$

where

$$\boldsymbol{K}_h = \int_{\Omega_0} \overline{\boldsymbol{N}}^t J \rho_{\mathrm{f}} \boldsymbol{\delta}^t \boldsymbol{B} \, \mathrm{d}\Omega_0 \tag{A.24}$$

$$\boldsymbol{\Phi}_h = \int_{\Omega_0} \overline{\boldsymbol{N}}^t J \rho_{\mathrm{f}} \frac{\phi^{\mathrm{f}}}{K_{\mathrm{f}}} \overline{\boldsymbol{N}} \, \mathrm{d}\Omega_0 \tag{A.25}$$

$$\overline{\boldsymbol{K}}_h = \int_{\Omega_0} \frac{J}{g} \boldsymbol{\Gamma}^t \left[\left(\boldsymbol{k} + \frac{k'}{\mu} \gamma_{\mathrm{f}} \left(1 - \phi^{\mathrm{f}} \right) \mathbf{1} \right) \cdot \left(\nabla^{\boldsymbol{x}} p_{\mathrm{f}} - \boldsymbol{\gamma}_{\mathrm{f}} \right) \right] \boldsymbol{\delta}^t \boldsymbol{B} \, \mathrm{d}\Omega_0$$
$$- \int_{\Omega_0} \frac{J}{g} \boldsymbol{\Gamma}^t \left[\boldsymbol{\epsilon} \left(\boldsymbol{k} \cdot \left(\nabla^{\boldsymbol{x}} p - \boldsymbol{\gamma}_{\mathrm{f}} \right) \right) + \boldsymbol{r} \left(k_{ik} p_{,j} \right) \right] \boldsymbol{B} \mathrm{d}\Omega_0 \tag{A.26}$$

$$\overline{\boldsymbol{\Phi}}_h = \int_{\Omega_0} \frac{J}{g} \boldsymbol{\Gamma}^t \boldsymbol{k} \left[\frac{1}{K_{\mathrm{f}}} \left(\nabla^{\boldsymbol{x}} p - \boldsymbol{\gamma}_{\mathrm{f}} \right) \overline{\boldsymbol{N}} + \boldsymbol{\Gamma} \right] \mathrm{d}\Omega_0, \tag{A.27}$$

and hence the incremental solution in equation (4.57).

References

[1] M. Mokni and J. Desrues. Strain localization measurements in undrained plane-strain biaxial tests on hostun rf sand. *Mechanics of Cohesive-Frictional Materials*, 4:419–441, 1998.

[2] T. Y. Lai, R. I. Borja, B. G. Duvernay, and R. L. Meehan. Capturing strain localization behind a geosynthetic-reinforced soil wall. *International Journal for Numerical and Analytical Methods in Geomechanics*, 27:425–451, 2003.

[3] A. Aydin. Fractures, faults, and hydrocarbon entrapment, migration and flow. *Marine and Petroleum Geology*, 17:797–814, 2000.

[4] J. R. Rice. On the stability of dilatant hardening for saturated rock masses. *Journal of Geophysical Research*, 80:1531–1536, 1975.

[5] J. W. Rudnicki. Formulation for studying coupled deformation pore fluid diffusion effects on localization of deformation. *AMD (Symposia Series) (American Society of Mechanical Engineers, Applied Mechanics Division)*, 57:35–44, 1983.

[6] J. W. Rudnicki. Effects of dilatant hardening on the development of concentrated shear

deformation in fissured rock masses. *Journal of Geophysical Research*, 89:9259–9270, 1984.

[7] S. L. Kramer. *Geotechnical Earthquake Engineering*. Prentice-Hall, New Jersey, 1996.

[8] K. Ishihara. Liquefaction and flow failure during earthquakes. *Géotechnique*, 43:351–415, 1993.

[9] G. Castro. Liquefaction of sands. *Harvard University, Harvard Soil Mechanics Series 81*, Jan 1969.

[10] F. Armero. Formulation and finite element implementation of multiplicative model of coupled poro-plasticity at finite strains under fully saturated conditions. *Computer Methods in Applied Mechanics and Engineering*, 171:205–241, 1999.

[11] J. H. Prevost and B. Loret. Dynamic strain localization in elasto-(visco-)plastic solids, part 2. Plane strain examples. *Computer Methods in Applied Mechanics and Engineering*, 83:275–294, 1990.

[12] J. Larsson and R. Larsson. Non-linear analysis of nearly saturated porous media: theoretical and numerical formulation. *Computer Methods in Applied Mechanics and Engineering*, 191:3885–3907, 2002.

[13] B. A. Schrefler, H. W. Zhang, M. Pastor, and O. C. Zienkiewicz. Strain localisation modeling and pore pressure in saturated sand samples. *Computational Mechanics*, 22:266–280, 1998.

[14] W. Ehlers, T. Graf, and M. Ammann. Deformation and localization analysis of partially saturated soil. *Computer Methods in Applied Mechanics and Engineering*, 193:2885–2910, 2004.

[15] B. Loret and J. H. Prevost. Dynamic strain localization in fuid-saturated porous media. *Journal of Engineering Mechanics, ASCE*, 117:907–922, 1991.

[16] R. Larsson, K. Runesson, and S. Sture. Embedded localization band in undrained soil based on regularized strong discontinuity—theory and fe-analysis. *International Journal of Solids and Structures*, 33:3081–3101, 1996.

[17] B. A. Schrefler, L. Sanavia, and C. E. Majorana. A multiphase medium model for localisation and postlocalisation simulation in geomaterials. *Mechanics of Cohesive-Frictional Materials*, 1:95–114, 1996.

[18] H. W. Zhang, L. Sanavia, and B. A. Schrefler. An internal lenght scale in dynamic strain localization of multiphase porous media. *Mechanics of Cohesive-Frictional Materials*, 4:443–460, 1999.

[19] P. Steinmann. A finite element formulation for strong discontinuities in fluid-saturated porous media. *Mechanics of Cohesive-Frictional Materials*, 4:133–152, 1999.

[20] M. Ortiz, Y. Leroy, and A. Needleman. A finite element method for localized failure analysis. *Computer Methods in Applied Mechanics and Engineering*, 61:189–214, 1987.

[21] Y. Leroy and M. Ortiz. Finite element analysis of strain localization in frictional materials. *International Journal for Numerical and Analytical Methods in Geomechanics*, 13:53–74, 1989.

[22] J. H. Prevost. Localization of deformations in elastic-plastic solids. *International Journal for Numerical and Analytical Methods in Geomechanics*, 8:187–196, 1984.

[23] R. I. Borja and R. A. Regueiro. Strain localization in frictional materials exhibiting displacement jumps. *Computer Methods in Applied Mechanics and Engineering*, 190:2555–2580, 2001.

[24] J. Desrues, R. Chambon, M. Mokni, and F. Mazerolle. Void ratio evolution inside shear bands in triaxial sand specimens studied by computed tomography. *Géotechnique*, 46:527–546, 1996.

[25] K. A. Alshibli, S. N. Batiste, and S. Sture. Strain localization in sand: plane strain versus triaxial compression. *Journal of Geotechnical and Geoenvironmental Engineering, ASCE*, 129:483–494, 2003.

[26] L. B. Wang, J. D. Frost, and J. S. Lai. Three-dimensional digital representation of granular material microstructure from X-Ray tomography imaging. *Journal of Computing in Civil Engineering, ASCE*, 18:28–35, 2004.

[27] A. L. Rechenmacher and R. J. Finno. Digital image correlation to evaluate shear banding in dilative sands. *Geotechnical Testing Jounal, ASCE*, 27:1–10, 2004.

[28] A. L. Rechenmacher. Grain-scale processes governing shear band initiation and evolution in sands. *Journal of the Mechanics and Physics of Solids*, 54:22–45, 2006.

[29] J. E. Andrade and R. I. Borja. Capturing strain localization in dense sands with random density. International Journal for Numerical Methods in Engineering, in press, 2006.

[30] R. I. Borja and J. E. Andrade. Critical state plasticity, Part VI: Meso-scale finite element simulation of strain localization in discrete granular materials. *Computer Methods in Applied Mechanics and Engineering*, 2006. In press for the John Argyris Memorial Special Issue.

[31] M. G. Jefferies. Nor-Sand: a simple critical state model for sand. *Géotechnique*, 43:91–103, 1993.

[32] K. Been and M. G. Jefferies. A state parameter for sands. *Géotechnique*, 35:99–112, 1985.

[33] D. M. Wood. *Soil Behaviour and Critical State Soil Mechanics*. Cambridge University Press, Cambridge, UK, 1990.

[34] R. M. Bowen. Theory of mixtures. In A. C. Eringen, editor, *Continuum Physics*, volume III—Mixtures and EM Field Theories, New York, NY, 1976. Academic Press.

[35] R. J. Atkin and R. E. Craine. Continuum theories of mixture: basic theory and historical development. *Quarterly Journal of Mechanics and Applied Mathematics*, 29:209–244, 1976.

[36] C. Li, R. I. Borja, and R. A. Regueiro. Dynamics of porous media at finite strain. *Computer Methods in Applied Mechanics and Engineering*, 193:3837–3870, 2004.

[37] F. Armero and C. Callari. An analysis of strong discontinuities in a saturated poro-plastic solid. *International Journal for Numerical Methods in Engineering*, 46:1673–1698, 1999.

[38] C. Callari and F. Armero. Analysis and numerical simulation of strong discontinuities in finite strain poroplasticity. *Computer Methods in Applied Mechanics and Engineering*, 193:2941–2986, 2004.

[39] J. Bear. *Dynamics of Fluids in Porous Media*. American Elsevier Publishing Company, Inc., New York, NY, 1972.

[40] O. C. Zienkiewicz and R. L. Taylor. *The Finite Element Method*, volume 1. Butterworth-Heinemann, Oxford, UK, fifth edition, 2000.

[41] T. J. R. Hughes. *The Finite Element Method*. Prentice-Hall, Englewood Cliffs, NJ, 1987.

[42] L. E. Malvern. *Introduction to the Mechanics of a Continuous Medium*. Prentice-Hall, Inc., Englewood Cliffs, NJ, 1969.

[43] J. E. Marsden and T. J. R. Hughes. *Mathematical Theory of Elasticity*. Prentice-Hall, Englewood Cliffs, NJ, 1983.

[44] J. H. Prevost. Mechanics of continuous porous media. *International Journal of Engineering Science*, 18:787–800, 1980.

[45] R. I. Borja. Cam-Clay plasticity, Part V: A mathematical framework for three-phase deformation and strain localization analyses of partially saturated porous media. *Computer Methods in Applied Mechanics and Engineering*, 193:5301–5338, 2004.

[46] O. Coussy. *Mechanics of Porous Continua*. John Wiley & Sons Ltd, West Sussex, UK, 1995.

[47] A. Nur and J. D. Byerlee. An exact effective stress law for elastic deformation of rock with fluids. *Journal of Geophysical Research*, 76:6414–6419, 1971.

[48] R. I. Borja. On the mechanical energy and effective stress in saturated and unsaturated porous continua. *International Journal of Solids and Structures*, 43:1764–1786, 2006.

[49] K. Terzaghi. *Theoretical Soil Mechanics*. John Wiley & Sons Ltd, New York, NY, 1943.

[50] E. H. Lee. Elastic-plastic deformation at finite strain. *Journal of Applied Mechanics*, 36:1–6, 1969.

[51] G. T. Houlsby. The use of a variable shear modulus in elasto-plastic models for clays. *Computers and Geotechnics*, 1:3–13, 1985.

[52] R. I. Borja, C. Tamagnini, and A. Amorosi. Coupling plasticity and energy-conserving elasticity models for clays. *Journal of Geotechnical and Geoenvironmental Engineering, ASCE*, 123:948–957, 1997.

[53] R. I. Borja and C. Tamagnini. Cam-Clay plasticity, Part III: Extension of the infinitesimal model to include finite strains. *Computer Methods in Applied Mechanics and Engineering*, 155:73–95, 1998.

[54] G. Gudehus. Elastoplastische stoffgleichungen fur trockenen sand. *Ingenieur-Archiv*, 42:151–169, 1973.

[55] J. H. Argyris, G. Faust, J. Szimmat, E. P. Warnke, and K. J. Willam. Recent developments in the finite element analysis of prestressed concrete reactor vessels. *Nuclear Engineering and Design*, 28:42–75, 1974.

[56] J. Jiang and Pietruszczak. Convexity of yield loci for pressure sensitive materials. *Computers and Geotechnics*, 5:51–63, 1988.

[57] K. J. Willam and E. P. Warnke. Constitutive model for the triaxial behaviour of concrete. In *Concrete Structures Subjected to Triaxial Stresses*, Bergamo, Italy, May 1974. ISMES.

[58] P. Pivonka and K. Willam. The effect of the third invariant in computational plasticity. *Engineering Computations*, 20:741–753, 2003.

[59] Y. F. Dafalias. Plastic spin: necessity or redundancy? *International Journal of Plasticity*, 14:909–931, 1998.

[60] A. Schofield and P. Wroth. *Critical State Soil Mechanics*. McGraw-Hill, New York, 1968.

[61] J. E. Andrade and R. I. Borja. Fully implicit numerical integration of a hyperelastoplastic model for sands based on critical state plasticity. In K. J. Bathe, editor, *Computational Fluid and Solid Mechanics 2005*, pages 52–54. Elsevier Science Ltd., 2005.

[62] O. C. Zienkiewicz, A. H. C. Chan, M. Pastor, B. A. Schrefler, and T. Shiomi. *Computational Geomechanics*. John Wiley & Sons Ltd, New York, NY, 1999.

[63] J. Kozeny. Über kapillare Leitung des Wassers im Boden. *Sitzungsberichte der Kaiserlichen Akademie der Wissenschaften in Wien*, 136:271–306, 1927.

[64] P. C. Carman. Fuid flow through a granular bed. *Transactions of the Institution of Chemical Engineers of London*, 15:150–156, 1937.

[65] T. Belytschko, W. K. Liu, and B. Moran. *Nonlinear Finite Elements for Continua and Structures*. John Wiley & Sons Ltd., West Sussex, UK, 2000.

[66] R. I. Borja and E. Alarcon. A mathematical framework for finite strain elastoplastic consolidation Part 1: Balance laws, variational formulation, and linearization. *Computer Methods in Applied Mechanics and Engineering*, 122:145–171, 1995.

[67] J. C. Simo. Algorithms for static and dynamic multiplicative plasticity that preserve the classical return mapping schemes of the infinitesimal theory. *Computer Methods in Applied Mechanics and Engineering*, 99:61–112, 1992.

[68] M. A. Murad and A. F. D. Loula. Improved accuracy in finite element analysis of Biot's consolidation problem. *Computer Methods in Applied Mechanics and Engineering*, 95:359–382, 1992.

[69] J. Wan. *Stabilized Finite Element Methods for Coupled Geomechanics and Multiphase Flow*. PhD thesis, Stanford University, Stanford, CA, 2002.

[70] M. A. Murad and A. F. D. Loula. On stability and convergence of finite element approximations of Biot's consolidation problem. *International Journal for Numerical Methods in Engineering*, 37:645–667, 1994.

[71] T. J. R. Hughes, L. P. Franca, and M. Balestra. A new finite element formulation for computational fluid dynamics: V. Circumvemting the Babuška-Brezzi condition. *Computer Methods in Applied Mechanics and Engineering*, 59:85–99, 1986.

[72] P. Mira, M. Pastor, T. Li, and X. Liu. A new stabilized enhanced strain element with equal order of interpolation for soil consolidation problems. *Computer Methods in Applied Mechanics and Engineering*, 192:4257–4277, 2003.

[73] J. C. Simo and M. S. Rifai. A class of mixed assumed strain methods and the method of incompatible modes. *International Journal for Numerical Methods in Engineering*, 29:1595–1638, 1990.

[74] R. I. Borja. Bifurcation of elastoplastic solids to shear band mode at finite strains. *Computer Methods in Applied Mechanics and Engineering*, 191:5287–5314, 2002.

[75] R. D. Holtz and W. D. Kovacs. *An Introduction to Geotechnical Engineering*. Prentice-Hall, Inc., Englewood Cliffs, NJ, 1981.

[76] H. W. Zhang and B. A. Schrefler. Particular aspects of internal lenght scales in strain localization analysis of multiphase porous materials. *Computer Methods in Applied Mechanics and Engineering*, 193:2867–2884, 2004.